Article:
Walkley, B., San Nicolas, R., Sani, M.A. et al. (2016) Phase evolution of C-(N)-A-S-H/N-A-S-H gel blends investigated via alkali-activation of synthetic calcium aluminosilicate precursors. Cement and Concrete Research, 89. pp. 120-135. ISSN: 0008-8846

https://doi.org/10.1016/j.cemconres.2016.08.010

Preprint of a paper published in *Cement and Concrete Research*, 89(2016):120-135. Version of record is available at http://dx.doi.org/10.1016/j.cemconres.2016.08.010

Phase evolution of C-(A)-S-H/N-A-S-H gel blends investigated via alkali-activation of synthetic calcium aluminosilicate precursors

Brant Walkley[1], Rackel San Nicolas[2], Marc-Antoine Sani[3], Gregory J. Rees[4], John V. Hanna[4], Jannie S.J. van Deventer[1, 5], John L. Provis[6]*

[1] *Department of Chemical and Biomolecular Engineering, The University of Melbourne, Victoria 3010, Australia*

[2] *Department of Infrastructure Engineering, The University of Melbourne, Victoria 3010, Australia*

[3] *School of Chemistry and Bio21 Institute, The University of Melbourne, Victoria 3010, Australia*

[4] *Department of Physics, The University of Warwick, Coventry CV4 7AL, United Kingdom*

[5] *Zeobond Pty Ltd, P.O. Box 23450, Docklands, Victoria 8012, Australia*

[6] *Department of Materials Science and Engineering, The University of Sheffield, Sheffield S1 3JD, United Kingdom*

* Corresponding author. Email: j.provis@sheffield.ac.uk, phone: +44 114 222 5490

Abstract

Stoichiometrically-controlled alkali-activated pastes containing calcium-(sodium) aluminosilicate hydrate (C-(N)-A-S-H) and sodium aluminosilicate hydrate (N-A-S-H) gels are produced by alkali-activation of high-purity synthetic calcium aluminosilicate powders. These powders are chemically comparable to the glass in granulated blast furnace slag, but without interference from minor constituents. The physiochemical characteristics of these gels depend on precursor chemical composition. Increased Ca content of the precursor promotes formation of low-Al, high-Ca C-(N)-A-S-H with lower mean chain length as determined by quantification of solid state nuclear magnetic resonance spectra, and less formation of calcium carboaluminate 'Alumino-ferrite monosulfate' (AFm) phases. Increased Al content promotes Al inclusion and reduced crosslinking within C-(N)-A-S-H, increased formation of calcium carboaluminate AFm phases, and formation of an additional N-A-S-H gel. Small changes in precursor composition can induce significant changes in phase evolution, nanostructure and physical properties, providing a novel route to understand microstructural development in alkali-activated binders and address key related durability issues.

Preprint of a paper published in *Cement and Concrete Research*, 89(2016):120-135. Version of record is available at http://dx.doi.org/10.1016/j.cemconres.2016.08.010

Keywords: Alkali-activated cement (D), aluminosilicate powder synthesis, calcium-silicate-hydrate (C-S-H) (B), spectroscopy (B)

1. Introduction

Alkali-activated materials (AAMs) offer a viable low-CO_2 alternative to Portland cement (PC) in numerous applications and exhibit desirable physical properties, as well as a potential reduction in CO_2 emissions by as much as 80% [1]. Coexistence of both sodium- and aluminium-substituted calcium silicate hydrate (C-(N)-A-S-H) and sodium aluminosilicate hydrate (N-A-S-H) gels, the main reaction products in AAM, results in complex thermodynamic and chemical interactions which dictate material properties and performance. Despite numerous studies investigating the chemistry of AAM, the literature is often conflicting and experimental analysis involves many unconstrained parameters. For this reason, it is necessary to use a method to study these materials that permits strict control of the stoichiometry in order to investigate relationships between precursor chemical composition and the molecular interactions governing phase evolution in AAM [2].

Previous approaches to this problem have involved synthesis of AAM precursor powders and binder phases in the laboratory under controlled conditions [3-7]. Of these, most use a sol-gel procedure to form aluminosilicate or calcium-aluminosilicate gels designed to simulate AAM binder phases and investigate the effect of alkali cations, alkaline earth cations or aluminium on C-S-H or N-A-S-H gels. This is done by addition of these ions after formation of the gel (either by direct addition of an ion source or by mixing two different gels together), which restricts the control of stoichiometry and homogeneity in these systems, as well as possibly modifying the structural roles of the cations. Additionally, the use of high amounts of water and the presence of nitrates in these studies can lead to differences in alkalinity and thus significantly affect the mechanisms of dissolution, reaction and phase formation [8, 9]. In most AAM systems, reactive species are initially present and participate simultaneously in the reaction. This leads to possible differences in the structure of the binder gel

networks formed when comparing the aforementioned synthetic gels to 'real-world' AAM systems if the degree of approach to thermodynamic equilibrium is restricted by transport or kinetic limitations.

Replication of the reaction conditions present during alkali-activation of reactive cementitious precursors has recently been achieved [10] by alkali-activation of high-purity synthetic aluminosilicate amorphous precursor powders synthesised via an organic steric entrapment solution-polymerisation route [11]. However, this has not previously been demonstrated for alkali-activation of calcium aluminosilicate precursors. Calcium is present to some extent in the majority of precursors used to produce AAMs, and is a primary constituent of blast furnace slag. Slag, however, contains significant quantities of MgO as well as numerous minor elements (e.g. Mn, Ti) which complicate dissolution and phase formation and possibly alter gel microstructure [12, 13]. Many slags also contain metal sulfides which can undergo redox processes and influence phase formation [14, 15]. Through the use of pure systems, key variables controlling phase formation can be isolated and controlled without the added complexity caused by the presence of additional minor constituents. Synthetic C-S-H and C-A-S-H systems have previously been produced via mixing CaO, SiO_2 and $CaO{\cdot}Al_2O_3$ in water and equilibrating over time [16-19], but to provide more accurate replication of the process of dissolution of chemical species from alkali-activated cement precursor particles, pure systems with lower water content must be examined.

In order to accurately replicate the reaction conditions present during alkali-activation of reactive cementitious precursors, this study utilises high-purity synthetic calcium aluminosilicate amorphous precursor powders synthesised via an organic steric entrapment solution-polymerisation route as described in detail previously [11], to develop a novel method of stoichiometric control of AAMs, following presentation of limited preliminary results in [20]. These AAMs are synthesised from the powder precursors under the same physicochemical conditions which prevail during alkali-activation of commonly used calcium aluminosilicate precursors such as ground granulated blast furnace slag (GGBFS) (i.e. reaction of an aluminosilicate precursor with an alkaline solution). The study presented

here extends this work utilising advanced characterisation techniques including ^{1}H, ^{29}Si, ^{27}Al, ^{23}Na solid state magic angle spinning (MAS) nuclear magnetic resonance (NMR) spectroscopy to provide a new level of insight into the role of precursor chemistry in phase evolution of C-(N)-A-S-H and N-A-S-H frameworks, as well as a detailed discussion of implications of these findings for AAM mix design.

2. Experimental Procedures

2.1 Alkali-activated material synthesis

Precursors were synthesised via an organic steric entrapment solution-polymerisation route [11], with compositions chosen to exhibit chemistry in regions of the quaternary $CaO - Na_2O - Al_2O_3 - SiO_2$ system which are important for studying C-(N)-(A)-S-H gels (Table 1). In particular, the Al/Si ratios represent values expected for non-crosslinked C-(N)-A-S-H (approximately Al/Si ≤ 0.10) and crosslinked C-(N)-A-S-H gels (approximately 0.10 ≤ Al/Si ≤ 0.20) [21-23]. The Al/Si and Ca/(Al+Si) ratios in the samples investigated here also span the range of bulk Al/Si and Ca/(Al+Si) ratios observed in $Na_2O{\cdot}xSiO_2{\cdot}yH_2O$ activated slags (Al/Si ≤ 0.25 and 0.67 ≤ Ca/(Al+Si) ≤ 1.2) [23-27] and laboratory synthesised C-A-S-H gels (Al/Si ≤ 0.2 and 0.5 ≤ Ca/(Al+Si) ≤ 1) [18, 21, 28-32]. The activating solution was prepared by dissolution of sodium hydroxide powder (AnalaR 99 wt %) in sodium silicate solution (N grade, 37.5 wt %, PQ Australia) and distilled water. Stoichiometry was designed to obtain an activating solution modulus of $SiO_2/Na_2O = 1$, with cation and water/solids (w/s) ratios as outlined in Table 1. The w/s ratios were chosen in order to achieve comparable paste consistency in all samples and setting within 3 days.

Preprint of a paper published in *Cement and Concrete Research*, 89(2016):120-135. Version of record is available at http://dx.doi.org/10.1016/j.cemconres.2016.08.010

Table 1: Empirical formula, Brunauer-Emmet-Teller surface area and D_{50} of the precursor (accurate to ± 2 m^2/g) and reaction mixture molar ratios for each sample

Precursor				Reaction mixture			
Sample	**Empirical formula**	**Surface area (m^2/g)**	**D_{50} (μm)**	**w/s**	**Ca/(Al+Si)**	**Al/Si**	**Na/Al**
A	$0.800CaO{\cdot}SiO_2{\cdot}0.078Al_2O_3$	2.90	23.7	0.75	0.67	0.15	0.50
B	$1.214CaO{\cdot}SiO_2{\cdot}0.078Al_2O_3$	3.82	40.1	1.00	1.00	0.15	0.50
C	$0.709CaO{\cdot}SiO_2{\cdot}0.0255Al_2O_3$	6.42	31.1	0.60	0.67	0.051	0.50
D	$1.104CaO{\cdot}SiO_2{\cdot}0.0255Al_2O_3$	3.58	36.7	0.75	1.00	0.051	0.50

The activating solution was mixed with the precursor powder to form a homogeneous paste which was subsequently cast in sealed containers cured at ambient temperature for 3, 28 and 180 days. Previous work has shown that the difference in w/s ratios didn't affect the degree of dissolution of the precursor powders [10, 20].

2.2 Characterisation

For all characterisation techniques except environmental scanning electron microscopy/energy dispersive X-ray spectroscopy (ESEM/EDX), the hardened pastes were ground by hand using a mortar and pestle and immersed in acetone to remove loosely bound water and halt the alkali-activation reaction. This method does not induce any significant changes in the AAM gel structure [33].

X-ray diffraction (XRD) experiments were performed using a Bruker D8 Advance instrument with Cu Kα radiation, a nickel filter, a step size of 0.020°, dwell time of 3 seconds and a 2θ range of 3 - 70°.

Environmental scanning electron microscopy (ESEM) was conducted using an FEI Quanta instrument with a 15 kV accelerating voltage and a working distance of 10 mm. To avoid the need to carbon coat the samples they were cut and immediately evaluated in low vacuum mode (0.5 mbar water pressure)

using a backscatter detector. A Link-Isis (Oxford Instruments) X-ray energy dispersive (EDX) detector was used to determine chemical compositions.

Attenuated total reflection Fourier transform infrared (ATR-FTIR) spectroscopy experiments were performed using a Varian FTS 7000 spectrometer with a Specac MKII Golden Gate single reflectance ATR attachment with KRS-5 optics and a diamond ATR crystal, collecting 32 scans at a resolution of 4 cm^{-1}.

Solid state single pulse ^{29}Si, ^{27}Al, ^{23}Na and ^{1}H MAS NMR spectra were collected on an Agilent VNMRS-600 spectrometer at 14.1 T (B_0) using a 4.0 mm triple resonance bioMAS probe. Parameters for each experiment are outlined in Table 2. ^{1}H-^{29}Si cross-polarisation (CP) MAS NMR experiments were collected on a Varian Infinity+ spectrometer at 7.05 T (B_0) using a 7.0 mm double resonance probe yielding a spinning frequency of 5 kHz, a ^{29}Si 'non selective' (solid) $\pi/2$ pulse width of 6.0 µs, an initial ^{1}H $\pi/2$ pulse width of 2.5 µs, a recycle delay of 4 s and Hartmann-Hahn contact periods of 4 ms. A nominal ^{1}H decoupling field strength of 80 kHz was employed during acquisition, and at least 20,000 transients were collected per experiment.

Data collected on the VNMRS-600 spectrometer were processed using NMRPipe [34], while data collected on the Varian Infinity+ spectrometer were processed using Bruker TopSpin. Deconvolution of the ^{29}Si MAS NMR spectra was performed using Gaussian peak profiles with assignments made with reference to the literature [35]. The minimum number of peaks possible was used to enable an accurate and meaningful interpretation of the spectra, and peak full width at half height was restricted to ≤ 4 ppm. Intensities of peaks were required to be consistent with the structural constraints described by the 'Crosslinked Substituted Tobermorite Model' (CSTM) for C-A-S-H products [23], and the thermodynamics of a statistical distribution of Si and Al sites within a Q^4 aluminosilicate network for N-A-S-H products [36].

Preprint of a paper published in *Cement and Concrete Research*, 89(2016):120-135. Version of record is available at http://dx.doi.org/10.1016/j.cemconres.2016.08.010

Table 2: Parameters for each single pulse MAS NMR experiment. Tetramethylsilane (TMS), powdered aluminium chloride hexahydrate ($AlCl_3 \cdot 6H_2O$) and powdered sodium chloride (NaCl) were used as reference compounds, as marked. * ^{27}Al MAS NMR experiments examining the precursors and alkali-activated material cured for 3 days were conducted with spinning speeds of 10kHz.

Nucleus	Field strength (T)	Transmitter frequency (MHz)	π/2 pulse width (μs)	Relaxation delay (s)	Scans	Spinning speed (kHz)	Reference (δ_{iso} / ppm)
^{29}Si	14.1	119.14	7.0	120	1024	10.0	TMS (0.0 ppm)
^{27}Al	14.1	156.26	4.0	2	1024	12.0*	$AlCl_3.6H_2O_{(s)}$ (0.0 ppm)
^{23}Na	14.1	158.63	5.0	3	512	12.0	$NaCl_{(s)}$ (7.2 ppm) [37]
^{1}H	14.1	599.70	2.7	3	32	12.0	$H_2O_{(l)}$ (4.7 ppm)

Preprint of a paper published in *Cement and Concrete Research*, 89(2016):120-135. Version of record is available at http://dx.doi.org/10.1016/j.cemconres.2016.08.010

3. Results and discussion

3.1 X-ray Diffraction

X-ray diffractograms of the precursor powders and AAMs cured for 3, 28 and 180 days are presented in Figure 1. Alkali-activation of all samples produces a broad feature centred at approximately 29° 2θ, characteristic of AAM and indicating formation of a disordered reaction product consistent with that formed during alkali-activation of GGBFS [13, 27], and increasing in intensity with reaction time. A broad peak at approximately 29° 2θ is assigned to a poorly crystalline C-(A)-S-H phase displaying some structural similarity with aluminium-containing tobermorite (PDF # 19-0052) [27], formed due to the dissolution and reaction of the amorphous phase from the precursor powder as well as C_2S (Ca_2SiO_4, Powder Diffraction File (PDF) cards: β polymorph # 33-0302 and α'_L polymorph PDF # 36-0642), C_3A ($Ca_3Al_2O_6$, cubic polymorph, PDF # 38-1429) and free lime (CaO, PDF # 48-1467) identified in the precursor powders.

AFm type phases in both the hemicarbonate (Hc, $Ca_4Al_2(OH)_{13}{\cdot}0.5CO_3{\cdot}xH_2O$) and monocarbonate (Mc, $Ca_4Al_2(OH)_{12}{\cdot}CO_3{\cdot}xH_2O$) forms are observed in alkali-activated samples A and B [38, 39], while the hydroxy-AFm phase (C_4AH_{13}) (PDF # 02-0077) forms in alkali-activated samples A, B and D. Small amounts of stilbite-Ca ($NaCa_2Al_5Si_{13}O_{36}.14H_2O$) (PDF # 44-1479) are also evident in AAM A. Vaterite (PDF # 33-0268) is present in alkali-activated sample D cured at all ages, while calcite (PDF # 47-1743) contributes a reflection at approximately 29.3 2θ in the X-ray diffractograms of all the AAMs.

The high calcium content in precursor B promotes the formation of portlandite ($Ca(OH)_2$) (PDF # 44-1481) as a reaction product, in addition to C-(A)-S-H, Hc/Mc and C_4AH_{13} products, during early stages of the reaction. Alkali-activation of the high-Al, high-Ca containing precursor for sample C also results in the formation of a small amount of portlandite due to hydration of C_2S which is largely consumed during the first 3 days of curing. Portlandite is progressively consumed as curing time increases and after 180 days reaction products (as observed by XRD) appear to be largely the same despite the initial

differences in Ca content of the precursors. Consumption of portlandite is driven by the pozzolanic reaction due to freely available silicon present in the reaction mixture, forming additional C-(A)-S-H [40]. ^{29}Si MAS NMR data discussed below (section 3.4.2) indicate that dissolution of Si from remnant precursor particles continues for up to 180 days and is the most likely reason for the progressive decrease in portlandite in samples B and C. An increase in calcite in these samples over the same time period suggests that carbonation is also contributing to the decrease in portlandite in these samples. Alkali-activation of the Ca-rich, Al-deficient precursor (sample D) does not result in the formation of portlandite, attributed to the low consumption of C_2S and free lime during alkali-activation of this precursor.

Greater Al content in the precursors promotes the formation of the Al-containing AFm reaction products. The reflections due to C_4AH_{13} and Mc in samples A and B decrease between 3 and 28 days of curing, and then increase significantly by 180 days of curing. The degree to which the intensity of these reflections changes with time is consistent for both samples, suggesting that similar reaction kinetics control phase evolution in each case. Formation of low Ca/Si C-(A)-S-H (due to release of Si from the precursor particles as discussed above) leads to a decrease in the level of dissolved Ca^{2+} ions, subsequent uptake of alkalis [40, 41] and a decrease in pH of the pore solution [42, 43] which results in destabilisation of Mc [44]. Replacement of C_4AH_{13} and Mc by Hc due to through-solution ion exchange followed by subsequent reaction of Hc with CO_3^{2-} to form Mc, as observed in fly ash/calcium aluminate cement blends [38, 45], will cause the observed changes in intensity of the C_4AH_{13} and Mc reflections. These trends are consistent with experimental observations and thermodynamic modelling of AFm phase evolution within alkali-activated slag and PC systems [38, 46-48].

Increased Ca content in the reaction mixture at Al/Si = 0.15 also promotes greater formation of C_4AH_{13} and Mc after 180 days. Greater calcium content in precursors with less Al content (Al/Si = 0.05) did not display this trend, with the only significant difference observable by XRD being a narrowing of the reflection of C-(A)-S-H. Reduced Al content in Ca-rich precursors has prevented the formation of

calcium carboaluminate phases and simultaneously reduced the amount of freely available Al which can substitute for Si within the C-(A)-S-H gel, consequently increasing the degree of structural order exhibited by this phase. This correlation of increasing structural order with increasing bulk Al content is consistent with observations for synthetic C-(N)-A-S-H samples [16, 17].

The reflection attributed to clinozoisite ($Ca_2Al_3(Si_2O_7)(SiO_4)O(OH)$, PDF # 44-1400) in the precursors for samples C and D remains unchanged after alkali-activation and 180 days of curing, suggesting that this phase remains inert and does not participate in the alkali-activation reaction. The reflection due to pavlovskyite ($Ca_8Si_5O_{18}$, PDF # 29-0368) identified in precursor C and D is absent from the AAMs, indicating dissolution of this phase upon alkali-activation. The reflection due to rosenhahnite ($Ca_3(Si_3O_8(OH_2))$, PDF # 29-0378) in the precursor of samples C and D increases upon alkali-activation and then remain unchanged beyond 3 days of curing. It is likely that the presence of rosenhahnite in the precursor has provided seed crystals and promoted nucleation to allow Ca^{2+} and silicates from the reaction mixture to participate in crystal growth during early stages of alkali-activation, after which growth is halted. Reflections due to stilbite do not appear to change between 3 and 180 days, suggesting that this phase does not participate in the reaction beyond 3 days.

Preprint of a paper published in *Cement and Concrete Research*, 89(2016):120-135. Version of record is available at http://dx.doi.org/10.1016/j.cemconres.2016.08.010

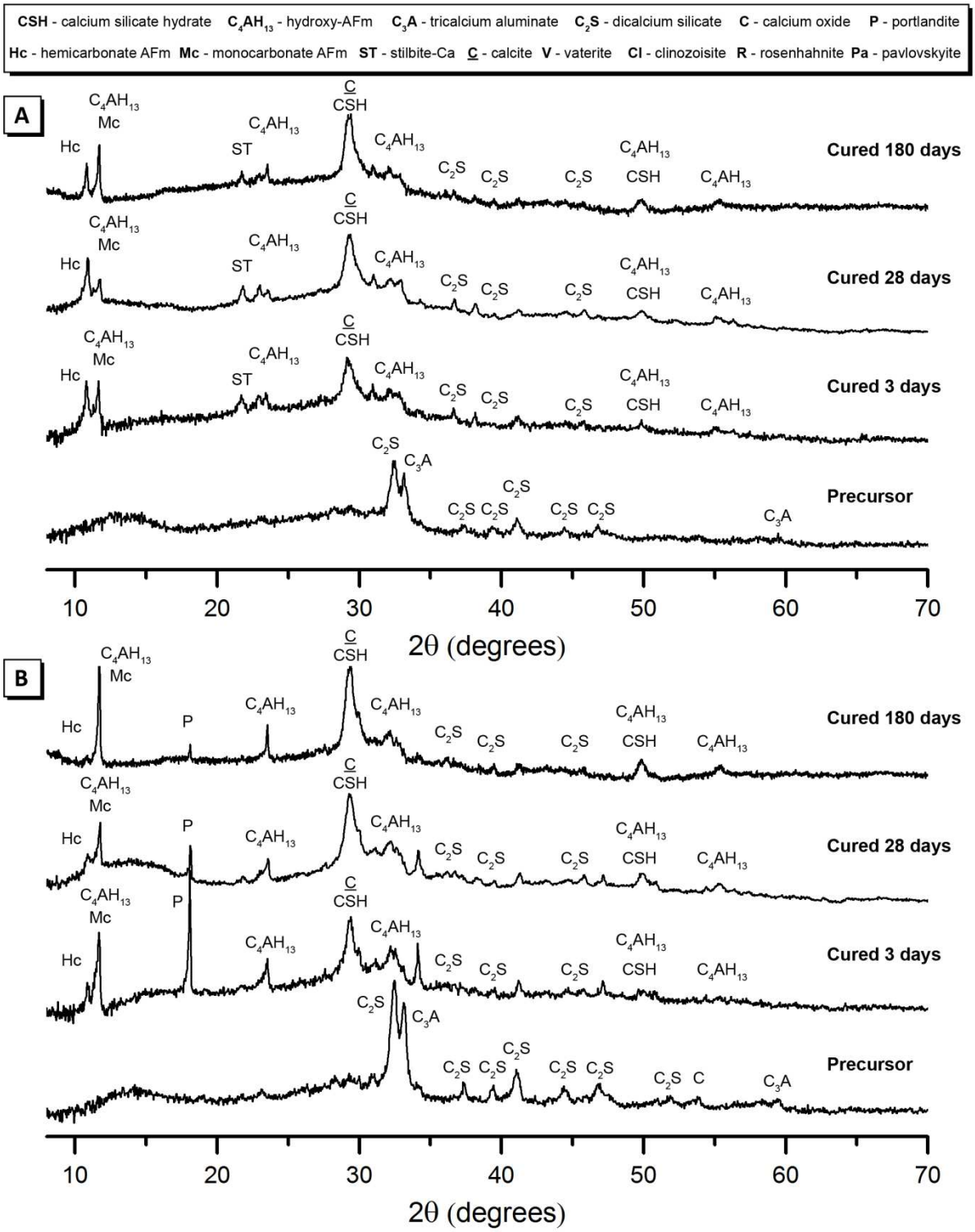

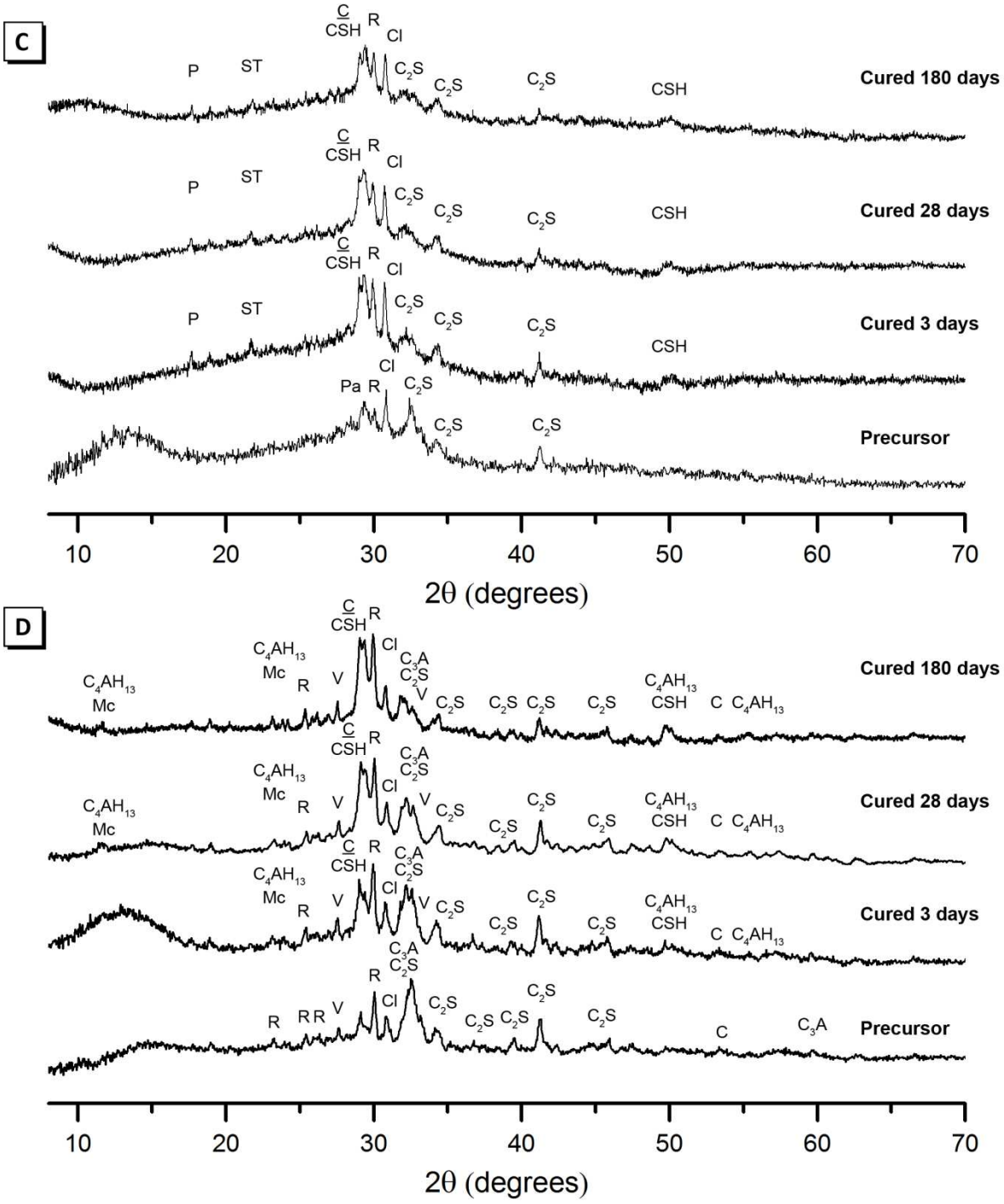

Figure 1: X-ray diffraction data for the precursor and alkali-activated material cured for 3, 28 and 180 days for samples A - D as marked.

3.2 Attenuated total reflectance Fourier transform infrared spectroscopy (ATR-FTIR)

ATR-FTIR spectra collected for the AAMs are presented in Figure 2; full interpretation of ATR-FTIR spectra of the precursors is provided in Appendix B, Supporting Information. Alkali-activation produces a broad intense band at approximately 950 cm^{-1} in the spectra of all samples cured for 3 days, attributed to asymmetric stretching vibrations of Si-O-T bonds (T: tetrahedral Si or Al) in the chain structure of C-(A)-S-H [5, 49, 50]. This band sharpens as curing time is increased, indicating that greater structural ordering of C-(A)-S-H evolves as the reaction proceeds. Increased curing time also sees a shift in this band to slightly lower wavenumbers in the spectra for samples A and B (Al/Si = 0.15) by 28 days, and then a shift to higher wavenumbers by 180 days. This indicates increased inclusion of Al within the C-(A)-S-H gel between 3 and 28 days followed by increased polymerisation and crosslinking of C-(A)-S-H, as well as a decrease in the Ca/Si ratio, between 28 and 180 days via condensation of tetrahedral species as a consequence of the increased Al content of the gel [51, 52].

A band at 666 cm^{-1} attributed to symmetrical stretching of Si-O-T bonds is observed in the spectra of the precursor (Appendix B, Supporting Information) and AAM for all samples, and remains unaltered over time. The sharp band at 870 cm^{-1} in the spectra of AAM A and B at all timepoints is associated with asymmetric stretching of AlO_4^- groups in Al-O-Si bonds within the C-(A)-S-H gel [50, 53]. The shift in the band initially present at 462 cm^{-1} in all samples to 424 cm^{-1} in samples A and B (Al/Si = 0.15), and to 440 cm^{-1} in samples C and D (Al/Si = 0.051), also suggests greater Al content within the silica network.

After 3 days of curing, the broad feature in the spectra of samples C and D (Al/Si = 0.15) attributed to asymmetric stretching vibrations of Si-O-T bonds in the chain structure of C-(A)-S-H is actually comprised of two bands (at 953 cm^{-1} and 928 cm^{-1} for sample C and 952 cm^{-1} and 928 cm^{-1} for sample D, see Appendix B, Supporting Information). This indicates a broad distribution of bond angles centred around two similar bond environments for each sample which can be attributed to Si-O-Si and Si-O-Al bonds, respectively [53, 54]. The sharpening of the vibration mode attributed to Si-O-T bonds within

C-(A)-S-H with increased curing time in all samples indicates increasing order of 8this phase, consistent with XRD observations (section 3.1), and this will be further analysed by NMR spectroscopy below.

Samples A and C, with lower calcium content, exhibit the highest wavenumbers for the band associated with Si-O-T bonds in the chain structure of C-(A)-S-H after 180 days of curing, suggesting that increased Al content within the reaction mixture increases the long term polymerisation and crosslinking of the C-(A)-S-H gel, consistent with thermodynamic modelling of sodium silicate-activated slag systems [23].

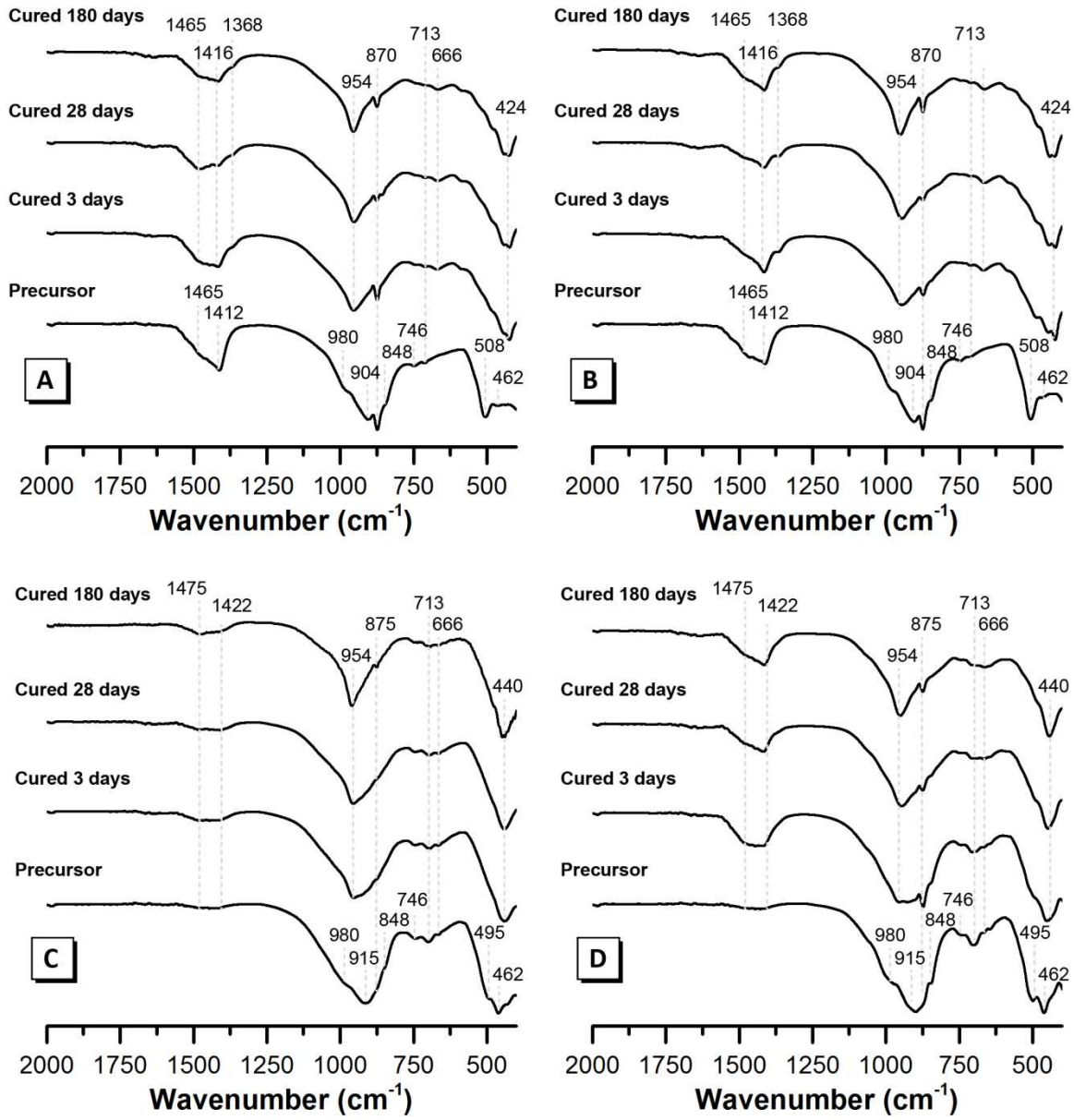

Figure 2: Infrared spectra (transmittance) of the precursor and alkali-activated material cured 3, 28 and 180 days for sample A - D as marked. The series of wavenumber labels closest to the spectra represent bands observed in the spectra of the precursor, whilst the series of wavenumber labels furthest from the spectra represent bands observed in the spectra of the alkali-activated material.

3.3 Environmental scanning electron microscopy/energy dispersive X-ray spectroscopy

Back-scattered electron (BSE) images for each sample (Figure 3 to 6) show a porous, particulate-structured AAM binder. Crystals displaying a plate-like morphology and elemental composition characteristic of AFm phases [56] are also observed in the BSE images and elemental maps for samples A and B cured for 180 days (Figure 3 and Figure 4).

The Mc phase previously identified by XRD is observed via elemental mapping of samples A and B at all ages, which show an Al-rich, Si- and Na- deficient crystalline phase containing a level of calcium which is not distinguishable from that of the background C-(A)-S-H (Figure 3 and Figure 4). No phases exhibiting similar morphology to known crystalline phases can be seen in the BSE image of sample C at any age. Some small (2 μm in length) plate-like crystals can be seen in the BSE images of sample D cured for 180 days (Figure 6). It is not possible to resolve the elemental composition of these crystals by EDX as their size is less than the depth of X-ray generation for the accelerating voltage used (15 keV) [57]. Consequently, they do not display discernibly different chemistry from the C-(A)-S-H phase when elemental maps are examined.

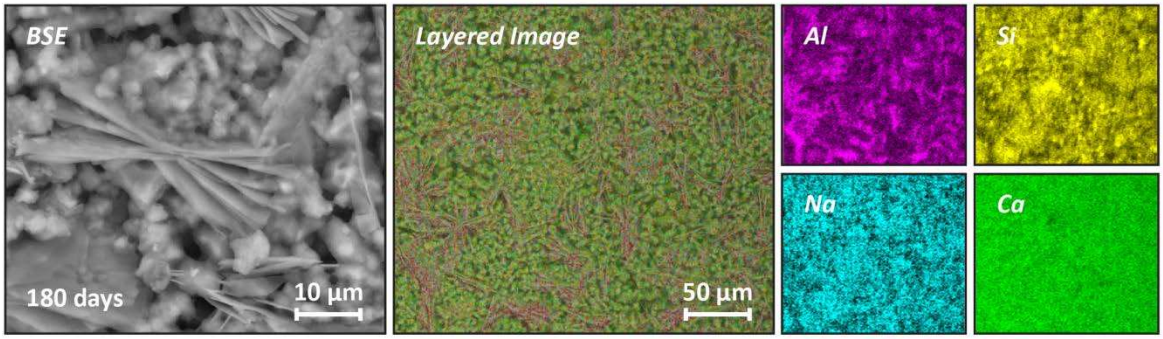

Figure 3: ESEM back-scattered electron (BSE) images and elemental maps of the alkali-activated sample A cured for 180 days.

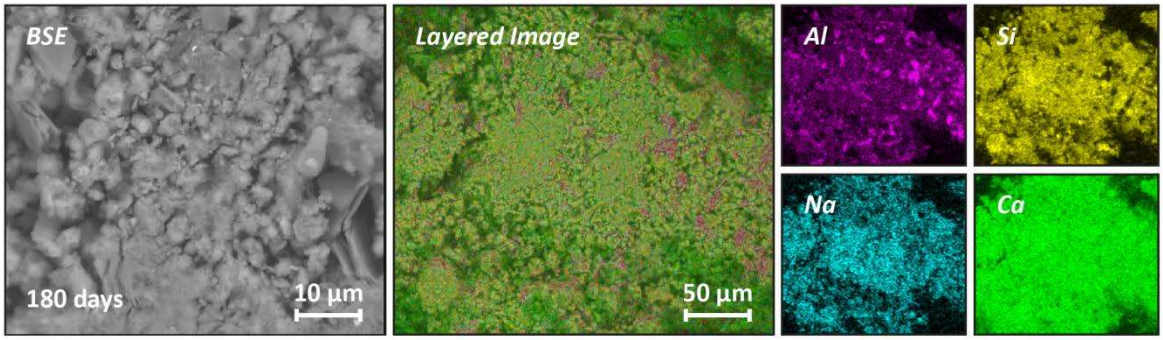

Figure 4: ESEM back-scattered electron (BSE) images and elemental maps of the alkali-activated sample B cured for 180 days.

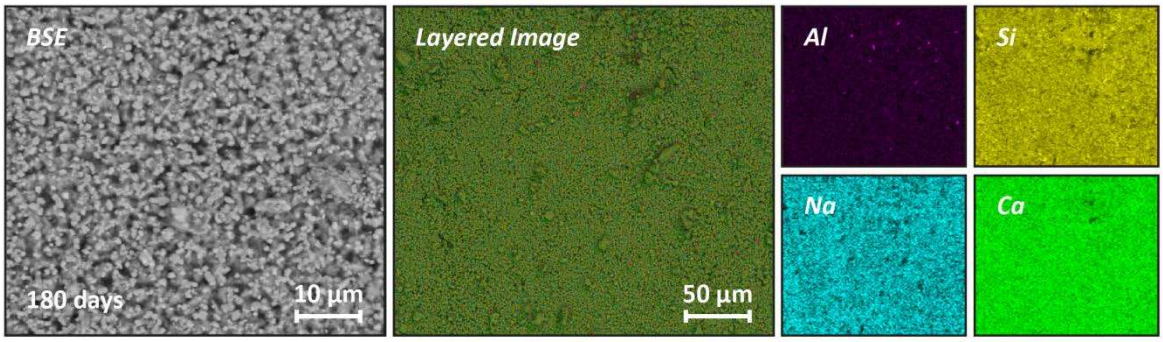

Figure 5: ESEM back-scattered electron (BSE) images and elemental maps of the alkali-activated sample C cured for 180 days.

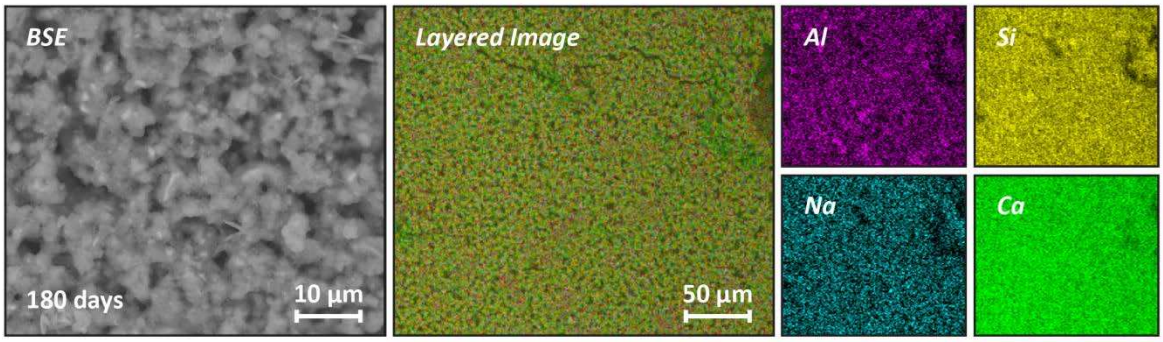

Figure 6: ESEM back-scattered electron (BSE) images and elemental maps of the alkali-activated sample D cured for 180 days.

The elemental composition of each sample as determined by ESEM – EDX is reported in Figure 7. The elemental composition is comparable with that of alkali-activated slag and slag/fly ash blends [52, 58] as well as that of synthetic C-(A)-S-H and N-A-S-H gels formed by a sol-gel method [6], and reveals important compositional changes induced by differences in reaction mix chemistry.

The chemistry of sample A cured for 3 days lies within the region commonly associated with a C-(N)-(A)-S-H) type gel, clustered along an imaginary line drawn between this region and the chemistry of AFm phases (Figure 7a i). At this age, the Na content is approximately the same for both samples A and B (Figure 7a ii and b ii), however sample B contains significantly greater Al content (Figure 7b i). Given that the reaction mixtures A and B contained equal amounts of Al, this suggests that distinct Al-rich reaction products have formed to a much greater extent in sample B than sample A, and in sample A it is likely that much of the Al exists within the N-A-S-H gel after 3 days; this is consistent with observations from ^{29}Si MAS NMR spectroscopy, see section 3.4.2. The higher bulk Ca content of sample B (Ca/(Al+Si) = 1.00) appears to have promoted greater formation of AFm phases and portlandite, in addition to C-(N)-A-S-H [6], consistent with XRD observations discussed in section 3.1, as well as greater inclusion of Al in the C-(N)-A-S-H binder [23, 29]. The lower bulk Ca content in the reaction mixture for sample A (Ca/(Al+Si) = 0.67) seems to promote formation of lower Ca, higher Na containing C-(N)-A-S-H. ^{29}Si MAS NMR data (discussed below) show the presence of N-A-S-H in addition to the C-(N)-A-S-H gel. This will be contributing to the reduction in bulk Ca content of the AAM in Figure 7. The main reaction product in both samples will be a mixture of C-(N)-A-S-H and N-A-S-H gels [23]; the low level of Ca in the reaction mixture will drive the substitution of Al and Na to form C-(N)-A-S-H gels to the maximum Al and Na incorporation that is thermodynamically stable [21, 23]. A decreased Ca/(Al+Si) ratio will drive the formation of N-A-S-H, while higher concentrations of Ca in the initial reaction mixture (as is the case for sample B) will drive further development of C-(N)-A-S-H.

For both samples C and D the chemistry of the AAMs lies within the region associated with C-(N)-A-S-H gels [23, 58]. For both samples, the binder cured for 3 days is more Ca-rich while containing the

approximately the same Al content as the reaction mixture, suggesting faster dissolution of Ca-rich phases from the precursor. The bulk Ca content in the reaction mixture for these samples is reflected in the chemistry of the binder cured for 3 days, with sample C (reaction mixture Ca/(Al+Si) = 0.67) appearing to consist of a C-(A)-S-H gel with low levels of Si, while sample D (reaction mixture Ca/(Al+Si) = 1.00) appears to consist of a C-(A)-S-H gel with moderate levels of Si, consistent with observations from FTIR as discussed in section 3.2.

After 28 days the chemistry of alkali-activated sample A is within the region associated with high Ca C-(N)-A-S-H gels (Figure 7a i), indicating a significant increase in Ca content consistent with further dissolution of C_2S as observed by XRD. Some data points for this sample cured for 180 days lie along a line linking the region associated with C-(N)-(A)-S-H composition and the composition of AFm phases (although heavily weighted toward the composition of C-(N)-A-S-H), consistent with the observation of these phases by XRD (section 3.1).

Curing for 28 days sees the chemistry of alkali-activated sample B shift to exhibit two distinct phases (Figure 7b); one exhibiting chemistry clustered along a line between C-(N)-A-S-H and the composition of AFm phases (heavily weighted towards C-(N)-A-S-H) and one exhibiting composition clustered along a line between C-(N)-(A)-S-H and the composition of portlandite (again heavily weighted towards C-(N)-A-S-H). The intimate mixture of C-(N)-A-S-H and AFm phases contains slightly more Al and approximately twice as much Na compared to the regions containing portlandite. By 180 days of curing, this sample exhibits a gel composition falling within the region assigned to moderate-Ca gels of the C-(N)-A-S-H type. After 180 days of curing the only discernible difference between the elemental compositions of the gels in samples A and B is the higher Al and Na concentrations in sample A.

Increased curing time does not significantly alter the elemental composition of the sample C and D (consistent with XRD observations, see section 3.1), however a narrowing of the compositional range exhibited by each binder is observed, suggesting that the reaction product in this sample after 180 days is either a single phase exhibiting narrowly distributed elemental compositions similar to that of

tobermorite-like C-(N)-A-S-H, or a very intimate mixture of C-(N)-A-S-H and N-A-S-H, rather than distinct and separate phases.

Overall, both low bulk Ca content (at constant Al/Si), and higher bulk Al content (at constant Ca/(Al+Si), promote increased formation of N-A-S-H and increased alkali uptake by C-(N)-A-S-H at early age, as indicated by Na/(Al+Si) ratio distributions on the Na_2O–Al_2O_3–SiO_2 ternary diagrams (Figure 7) and consistent with observations for synthetic C-(N)-A-S-H gels [16]. Increased Ca content in the precursor appears to impede formation of N-A-S-H and promote formation of Ca-rich C-(N)-A-S-H at early ages, with less formation of calcium carboaluminates, and little evolution of binder chemistry at late ages.

Preprint of a paper published in *Cement and Concrete Research*, 89(2016):120-135. Version of record is available at http://dx.doi.org/10.1016/j.cemconres.2016.08.010

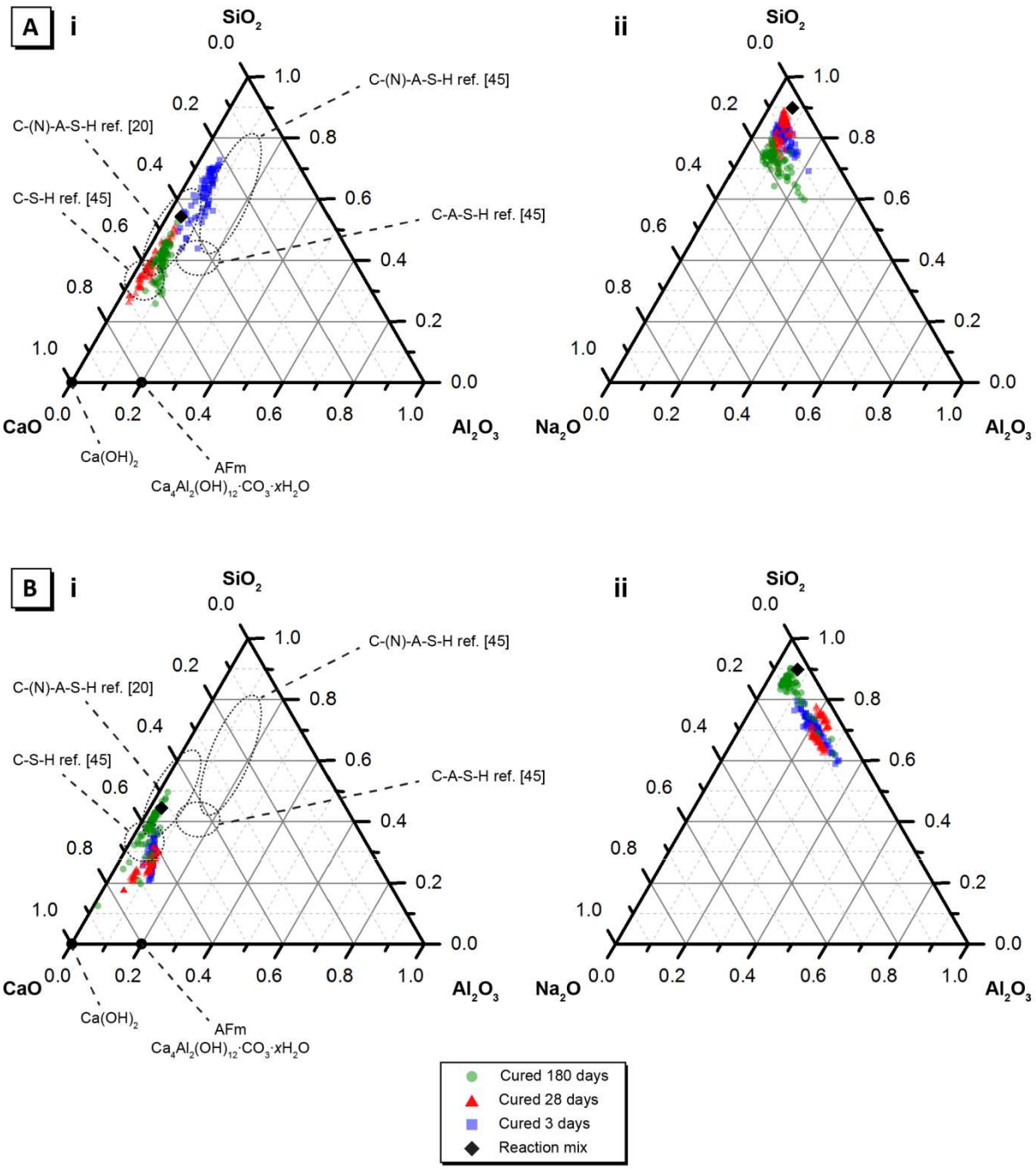

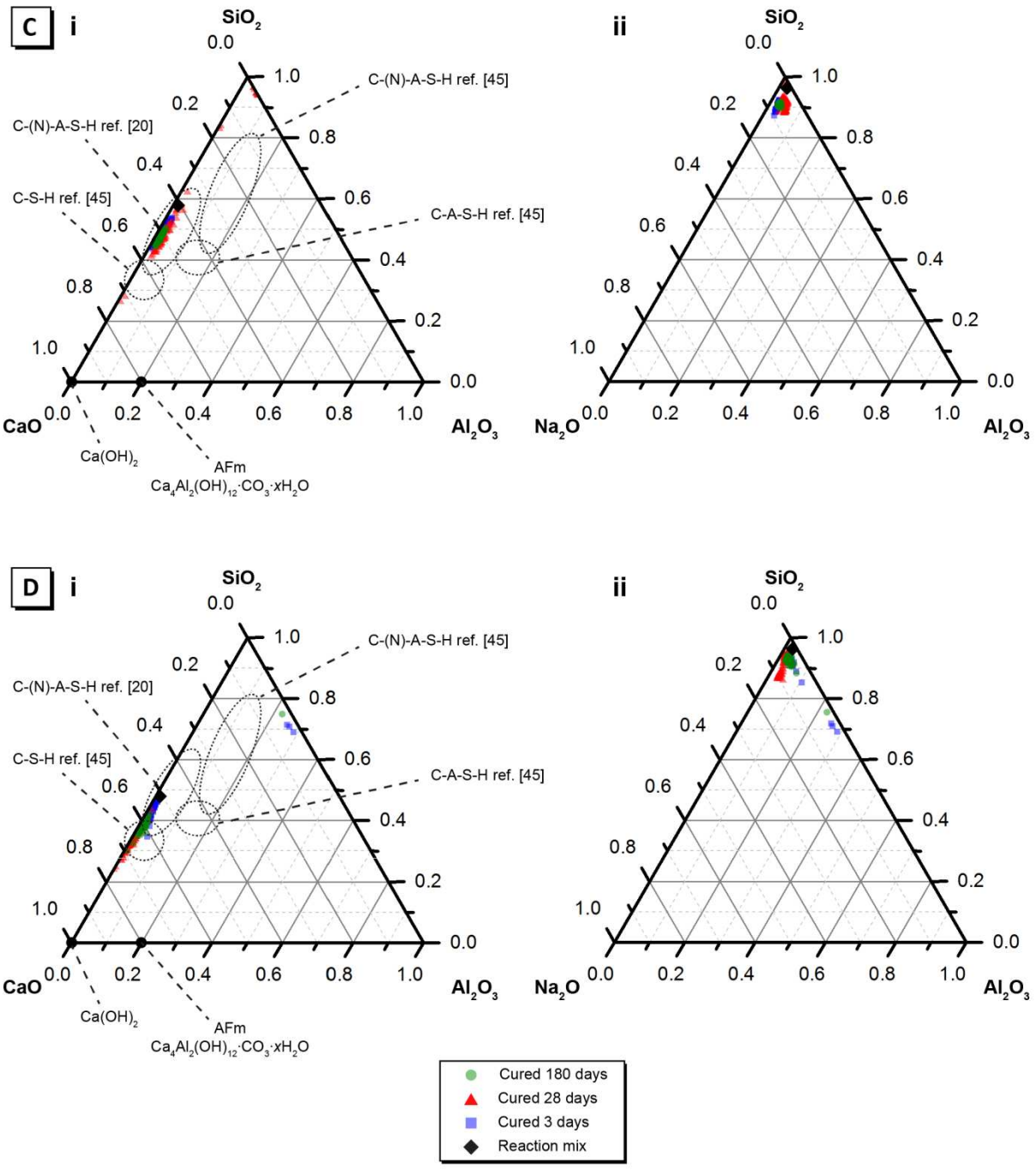

Figure 7: Projection of alkali-activated material chemistry onto the i) ternary CaO – Al_2O_3 – SiO_2 system (neglecting Na_2O content) and ii) ternary Na_2O – Al_2O_3 – SiO_2 system (neglecting CaO content) showing elemental composition of AAMs cured for 3, 28 and 180 days for samples A – D as marked, as determined by ESEM-EDX analysis. A random selection of points evenly distributed across a representative 500 µm × 500 µm section of the sample were used for analysis. A total of 60 individual points were collected per sample at each age. Approximate regions of C-S-H, C-(A)-S-H and C-(N)-A-S-H determined from [23] and [58].

3.4 Solid state magic angle spinning nuclear magnetic resonance spectroscopy

3.4.1 ^{27}Al MAS NMR

The ^{27}Al MAS NMR spectra for the precursors and AAMs for each sample are presented in Figure 8, and detailed characterisation of precursor powders has been previously reported [11]. The spectra of each precursor are very similar, displaying a broad tetrahedral AlO_4 resonance centred at approximately 57 ppm attributed to a distribution of Al environments within the glassy phase of the precursor (as identified by XRD), similar to that observed for GGBFS [13, 27]. The spectra of each precursor display a low intensity resonance centred at approximately 0 ppm, partly overlapping the spinning side band of the main Al(IV) peak, attributed to octahedral AlO_6. This is consistent with the small amount of C_3A identified by XRD in samples A, B and D [59]; the presence of this resonance in the spectra of precursor C suggests the presence of a small amount of poorly crystalline C_3A not identifiable by XRD.

The ^{27}Al MAS NMR spectra of each AAM cured for 3 days display a low intensity broad resonance spanning from 30 ppm to 70 ppm and centred at approximately 58 ppm, this is assigned to Al in a significantly distorted tetrahedral environment [25, 27, 60]. A low intensity narrow resonance at approximately 76 ppm assigned to Al in a well defined tetrahedral coordination, and a high intensity narrow resonance at approximately 11 ppm assigned to Al in a well defined octahedral coordination, are also observed in the spectra of the AAMs for samples A, B and D. Well structured crystalline C-(N)-A-S-H identified in the AAMs for each of these samples by XRD and ESEM-EDX will contain Al substituted for Si bridging sites in a tetrahedrally coordinated environment, leading to the well defined resonance observed at 76 ppm, while poorly crystalline C-(N)-A-S-H and amorphous N-A-S-H will contain Al in significantly distorted tetrahedral environments, leading to the broad resonance centred at approximately 58 ppm [25, 27, 60]. The AFm reaction products are responsible for the narrow resonance observed at 11 ppm [60, 61].

The resonance due to distorted Al(IV) environments in samples A and B (Al/Si = 0.15) shifts to higher ppm between 3 and 28 days and then shifts to lower ppm between 28 and 180 days, consistent with observations by FTIR of increased Al incorporation within the C-(N)-A-S-H gel between 3 and 28 days followed by increased Si incorporation within the C-(N)-A-S-H gel between 28 and 180 days. Increased Al incorporation within the C-(N)-(A)-S-H gel at an early age is favoured due to the preference of Al to be located in crosslinked and polymerised sites. At later ages, condensation reactions between depolymerised Si species within the C-(N)-A-S-H gel will occur and lead to further crosslinking, increasing the Si/Al ratio of the gel. The incongruent dissolution of the precursor particles with preferential early Al release, as identified above, will also be contributing to these trends.

For samples C and D (Al/Si = 0.05), increased curing time sees progressive deshielding of the distorted Al(IV) environments, indicating continued Al inclusion into C-(A)-S-H as the reaction progresses, consistent with more congruent dissolution of the Al and Si from the precursor. Early age preferential dissolution of Al appears to be promoted by increased Al content in the precursor [62]. In all samples, a narrowing of this resonance occurs with increased curing time, consistent with the rearrangement into a more ordered structure containing Al(IV) occurs as the reaction progresses.

The peak assigned to Al(VI) in AFm phases in samples A, B and D shifts slightly to lower ppm between 3 and 28 days (indicating increased electron density around the Al nucleus) and remains unaltered thereafter. A small resonance at 6 ppm is also observed in samples B and D (Ca/(Al+Si) = 1.00) cured for 28 and 180 days. The intensity of this resonance remains unaltered between 28 and 180 days in sample B and increases between 28 and 180 days in sample D. When this resonance is observed in PC hydrates, it is attributed to Al(VI) species within the 'third aluminate hydrate' (TAH), an amorphous nanoscale aluminate hydrate phase precipitated at the surface of the C-S-H type gels [61, 63, 64], and which has also been noted in alkali-activated slags [27, 60, 65]. The presence of TAH in samples B and D (Ca/(Al+Si)=1.00) and absence in samples A and C (Ca/(Al+Si)=0.67) is consistent with stoichiometric arguments and thermodynamic modelling which suggest that the presence of TAH is likely to be linked

to high concentrations of available Ca and Al [8, 15, 66]. It is interesting to note that in the samples examined here, increased Al content does not appear to increase the proportion of Al(VI) within TAH but rather promotes increased formation of crystalline AFm phases (monocarbonate, hemicarbonate and C_4AH_{13}). This could be due to steric limitations on the amount of TAH which can precipitate at the gel surface, or to preferential formation of TAH when there are insufficient quantities of OH^-, CO_3^{2-} or silicate anions required to form AFm phases.

Despite differing Al and Ca contents, the ^{27}Al MAS NMR spectra for each sample appear very similar, however close examination allows some important trends to be identified. For all binders, when Si and Al content are held constant, increased Ca content results in increased Al incorporation within the C-(N)-(A)-S-H gel. When Si and Ca content are held constant (i.e. comparing sample A with C and sample B with D), increased Al content also results in deshielding of Al, indicating increased Al incorporation within the C-(A)-S-H gel. These trends are reflected in the chemical shift exhibited by the main distorted Al(IV) peak for each sample cured for 180 days - sample A: 60.5 ppm, sample B: 64.5 ppm, sample C: 59.0 ppm, sample D: 63.0 ppm.

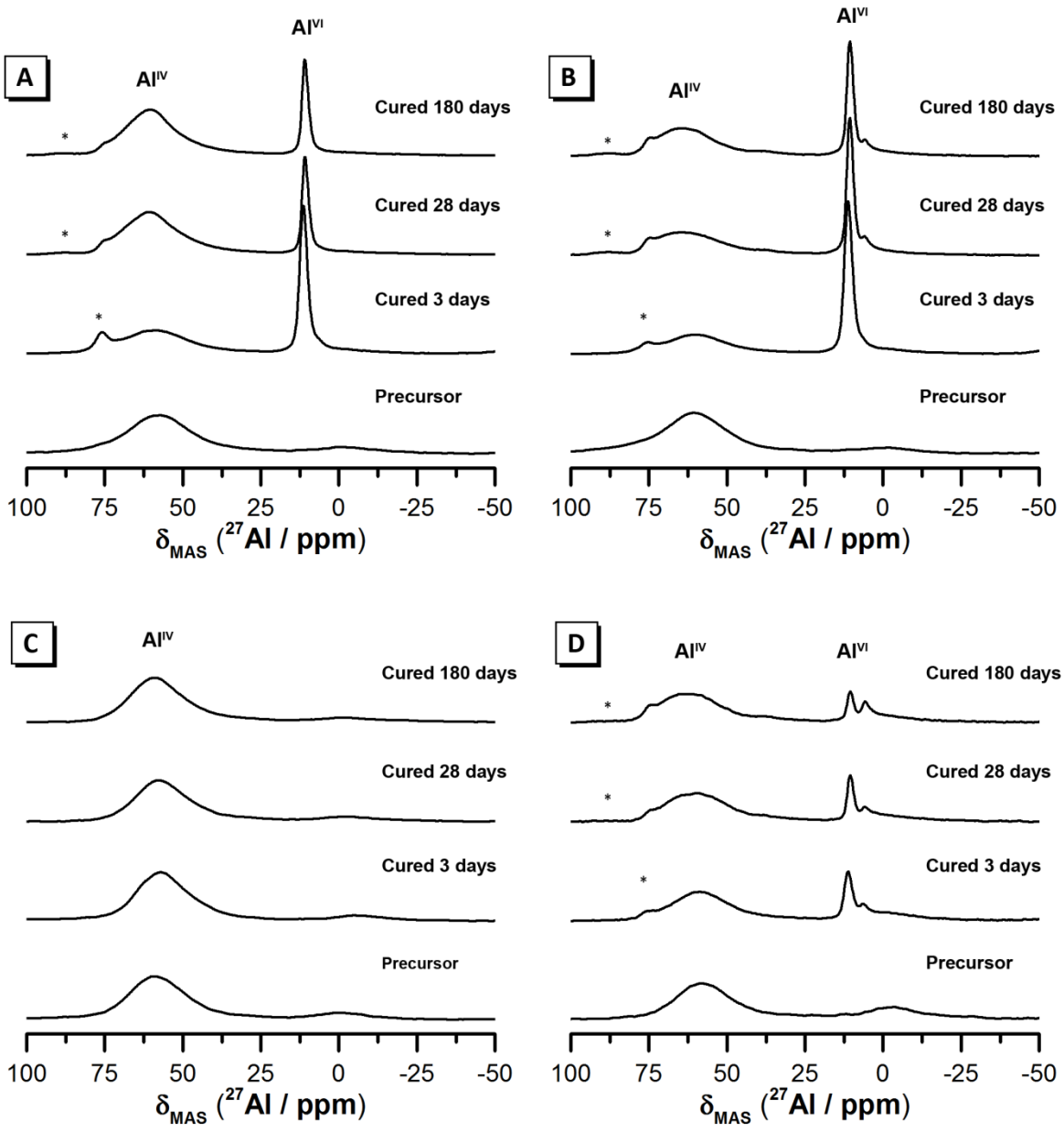

Figure 8: ^{27}Al MAS (12 kHz) NMR spectra (ν_0 = 156.26 MHz) of the precursor and alkali-activated material cured for 3, 28 and 180 days as marked for a) sample A, b) sample B, c) sample C and d) sample D. Positions at which spinning side bands are expected are indicated by *.

3.4.2 ^{29}Si MAS NMR

The ^{29}Si MAS NMR spectra for each precursor and AAM are presented in Figure 9. Deconvolutions of the precursor spectra have been previously reported [11] while deconvolutions of the AAM spectra

are summarised in Table 3 (full details provided in Appendix C, Supporting Information). Each precursor consists predominantly of Q^2, Q^2(1Al), Q^3 and Q^3(1Al) sites within a depolymerised calcium silicate phase as well as smaller amounts of Q^4, Q^4(1Al) and Q^4(2Al) within a highly polymerised aluminosilicate phase [11]. Q^0 and Q^1 are also observed within low Al-containing precursors C and D and are attributed to C_2S and clinozoisite, respectively [61].

Alkali-activation of each sample results in formation of six new Si environments indicated by peaks at approximately −76 ppm, −79 ppm, −82 ppm, −85 ppm, −88 ppm and −94 ppm, attributed to Q^0, Q^1, Q^2(1Al), Q^2, Q^3(1Al), and Q^3, respectively, within a C-(N)-A-S-H gel, with at least some degree of crosslinking occurring in each sample as evidenced by the Q^3 and Q^3(1Al) sites [8, 23, 27, 67]. In all samples alkali-activation results in a narrowing of the resonances attributed to Q^2(1Al), Q^2, Q^3(1Al), and Q^3 species, indicating that these environments are more ordered within the C-(N)-A-S-H gel than within the depolymerised calcium aluminosilicate phase of the precursors. For all samples, increased curing time results in a narrowing of the resonances attributed to Q^1, Q^2(1Al), Q^2, and Q^3(1Al) species, indicating increased ordering within C-(N)-(A)-S-H as the reaction proceeds. Formation of Q^4(4Al) and Q^4(3Al) sites within a polymerised Al-rich aluminosilicate phase is also observed upon alkali-activation of all samples, and is most pronounced in samples A and C (with Ca/(Al+Si)=0.67), as discussed in more detail below and in Appendix C, Supporting Information.

Preprint of a paper published in *Cement and Concrete Research*, 89(2016):120-135. Version of record is available at http://dx.doi.org/10.1016/j.cemconres.2016.08.010

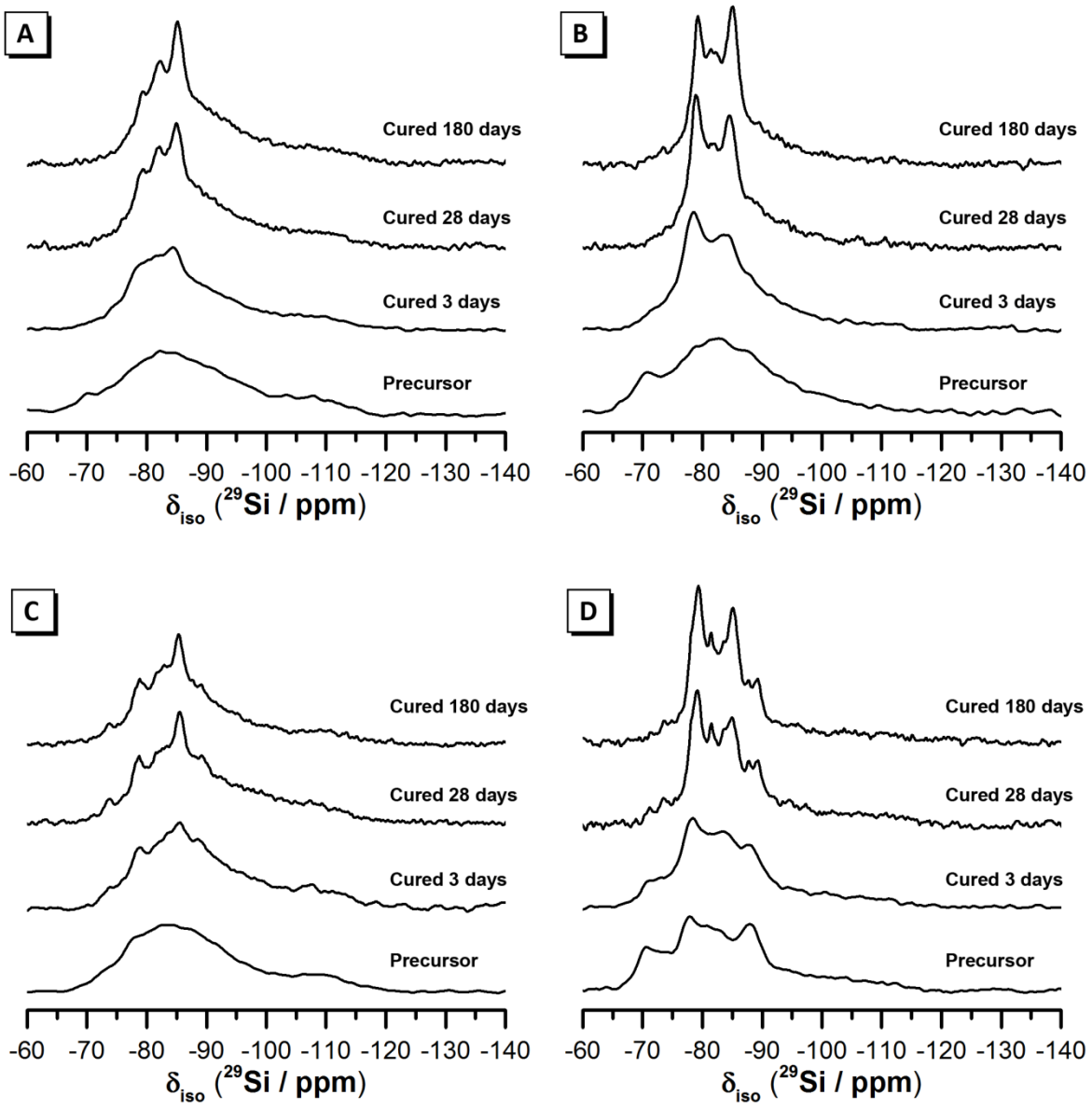

Figure 9: ^{29}Si MAS (10 kHz) NMR spectra (ν_0 =119.14 MHz) of the precursor and alkali-activated material for samples A-D cured for 3, 28 and 180 days as marked.

Table 3: Summary of $Q^n(mAl)$ Si coordination environments within the reaction product identified in the deconvoluted ^{29}Si MAS NMR spectra for each AAM material as a function of curing time. Estimated uncertainty in absolute site percentages is ± 2%. Absolute site percentages attributed to remnant precursor are omitted for clarity.

Sample A	***Reaction products (%)***						
Curing time (days)	**Q^1**	**$Q^2(1Al)$**	**Q^2**	**$Q^3(1Al)$ + $Q^4(4Al)$**	**Q^3**	**$Q^4(3Al)$**	**$Q^4(2Al)$**
3	6	18	9	10	1	8	0
28	8	13	19	8	1	11	0
180	7	12	21	9	1	12	0

Sample B	***Reaction products (%)***						
Curing time (days)	**Q^1**	**$Q^2(1Al)$**	**Q^2**	**$Q^3(1Al)$ + $Q^4(4Al)$**	**Q^3**	**$Q^4(3Al)$**	**$Q^4(2Al)$**
3	11	11	7	4	1	1	0
28	18	12	17	5	1	3	0
180	18	15	25	6	1	6	0

Sample C	***Reaction products (%)***						
Curing time (days)	**Q^1**	**$Q^2(1Al)$**	**Q^2**	**$Q^3(1Al)$ + $Q^4(4Al)$**	**Q^3**	**$Q^4(3Al)$**	**$Q^4(2Al)$**
3	7	13	7	15	1	10	3
28	7	14	10	14	1	9	3
180	8	16	13	15	1	10	0

Sample D	***Reaction products (%)***						
Curing time (days)	**Q^1**	**$Q^2(1Al)$**	**Q^2**	**$Q^3(1Al)$ + $Q^4(4Al)$**	**Q^3**	**$Q^4(3Al)$**	**$Q^4(2Al)$**
3	8	7	5	3	0	2	0
28	13	10	13	8	1	2	0
180	19	14	21	10	1	3	0

Difference ^{29}Si MAS NMR spectra for each AAM cured for 3 days, obtained by subtraction of the precursor spectra from those of the hardened products, are shown in Figure 10. This provides information about the net consumption (indicated by regions of negative intensity) and net production (indicated by regions of positive intensity) of different Si species during alkali-activation of each sample.

Alkali-activation of each precursor causes significant reduction in intensity of the Q^0 and Q^1 regions of the spectra (−65 ppm to −75 ppm) as well as a slight reduction in intensity in the region associated with Al-substituted Q^4 silicon coordination environments (−88 ppm to −110 ppm) in samples A and B.

This suggests preferential dissolution of Q^0 and Q^1 environments from the depolymerised calcium silicate phase within the precursor has occurred during alkali-activation of these samples. A significant increase in intensity is observed between −75 ppm and −88 ppm, consistent with formation of the C-(N)-A-S-H gel identified above. Low Al-substituted Q^2 and Q^3 species present within each precursor will also be consumed during alkali-activation, however this is not reflected by negative intensity within the region of these resonances in Figure 10, suggesting that the amount of new Q^2, Q^2(1Al), Q^3 and Q^3(1Al) Si species produced during alkali-activation is likely to be significantly higher than is indicated by the net positive intensity these regions.

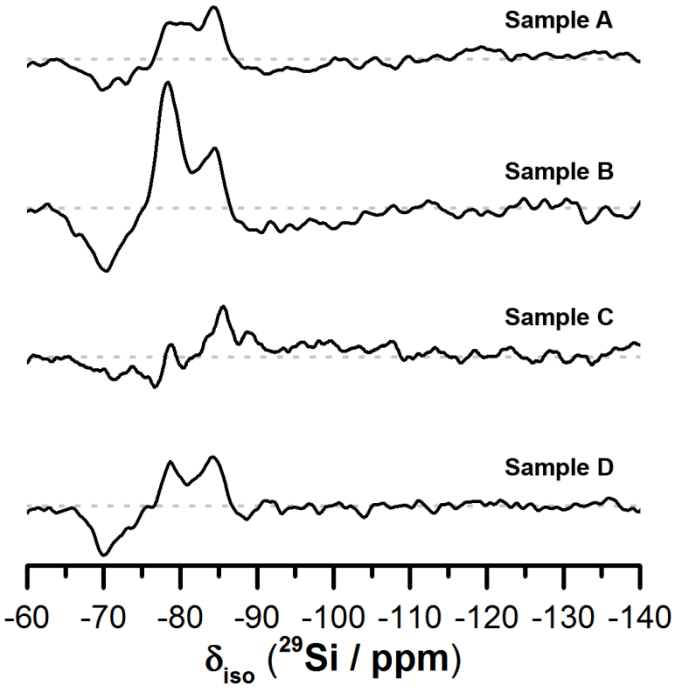

Figure 10: Difference plots generated by subtracting the ^{29}Si MAS NMR spectrum of each respective anhydrous precursor from the corresponding spectra of the alkali-activated materials cured for 3 days. Baselines are indicated by the grey dotted lines to allow identification of resonances with positive intensity (indicating net production of these species during alkali-activation) and resonances with negative intensity (indicating net consumption of these species during alkali-activation).

Single-pulse ^{29}Si MAS NMR and ^{1}H-^{29}Si cross polarisation (CP) MAS NMR spectra of the precursor and AAM for sample A are shown in Figure 11. ^{1}H-^{29}Si CP MAS NMR spectra indicate the Si species closely associated with water (i.e. Si-OH linkages) that are likely to exist as part of the C-(N)-A-S-H gel or AFm phases [8, 68]. The ^{1}H-^{29}Si CP MAS NMR spectrum exhibits greater relative intensity than the single-

pulse ^{29}Si MAS NMR spectrum in the region attributed to the hydrous Q^1, $Q^2(1Al)$, Q^2 and $Q^3(1Al)$ Si sites of the C-(N)-A-S-H gel (−75 ppm to −88 ppm). Conversely, the reduction in relative intensity of the ^{1}H-^{29}Si CP MAS NMR spectrum compared with the single-pulse ^{29}Si MAS NMR spectrum in the region attributed to Al-substituted Q^4 species (−88 ppm to −120 ppm) indicates that these environments are anhydrous. The trends observed for sample A during alkali-activation are likely to be occurring for all samples.

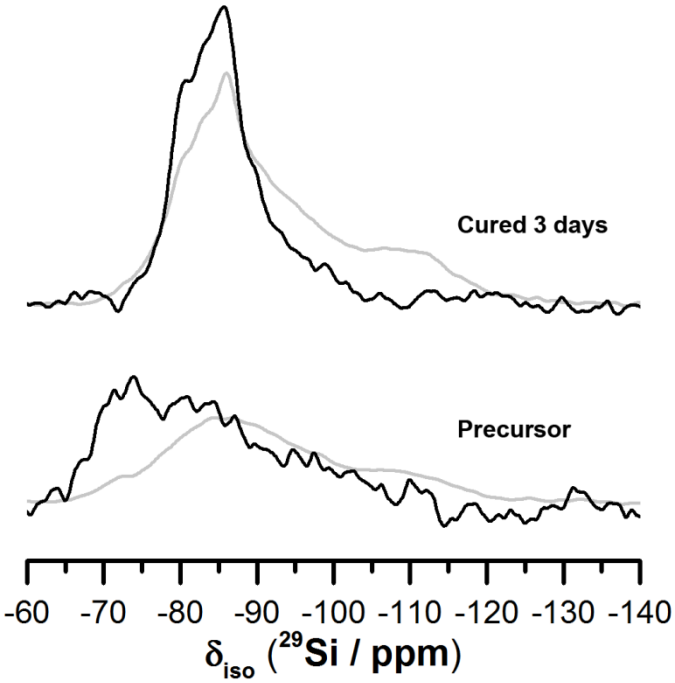

Figure 11: Single-pulse ^{29}Si (grey) and ^{1}H - ^{29}Si cross polarisation (CP) (black) MAS NMR spectra (collected at 56.61 MHz with a spinning speed of 5 kHz) of the precursor and alkali-activated material cured for 3 days for sample A. All spectra are normalised to constant total intensity (area under the curve) from –50 to –150 ppm to enable relative comparison.

Due to the presence of numerous phases within the precursors, as well as previous observations of preferential dissolution of Al over Si from aluminosilicate precursors produced using the same synthesis method [10], it is unlikely that congruent dissolution of the various Si coordination environments from the precursor will occur during alkali-activation. Rather, it is likely that dissolution of the depolymerised calcium silicate phase previously identified in the precursors [11] will occur faster than dissolution of the highly polymerised aluminosilicate phase. Using this observation, it is

thus possible to simulate the change in intensity of resonances in the ^{29}Si MAS NMR spectra due to consumption of individual Si species from each precursor phase, and use Gaussian peak profiles to deconvolute the ^{29}Si MAS NMR spectra of the AAMs. Relative quantification of each species identified in the deconvolutions at all timepoints is shown in Table 3.

Upon alkali-activation of low-Ca precursors (samples A and C, Ca/(Al+Si)=0.67), increased Al content in the precursor of sample A results in a decrease in crosslinking species while exhibiting similar Al substitution within the C-(N)-A-S-H gel (Table 3). This can be attributed to the capacity for Al substitution into crosslinked species [21]. Consequently, increased Al content promotes the formation of non-crosslinking Q^2(1Al) species within the C-(N)-A-S-H gel and results in an overall decrease in the extent of crosslinking. In both samples, increased curing time promotes greater polymerisation (increased Q^2 sites) while the extents of crosslinking and Al substitution within the C-(N)-A-S-H gel remain largely the same. This is consistent with observations by FTIR (section 3.2) as well as ^{27}Al MAS NMR (section 3.4.1) as discussed above, and is commonly observed for silicate-activated slag [21], however is contrary to observations for synthetic C-(N)-A-S-H [16].

Alkali-activation of high-Ca precursors (sample B and D, Ca/(Al+Si)=1.00) results in formation of mainly Q^1 and Q^2(1Al) sites, with smaller amounts of Q^2, Q^3(1Al) and Q^3. Continued curing sees significantly increased polymerisation in both samples, indicated by a large increase in Q^2 sites. A decrease in Al substitution with time is observed in Sample B, while the Al content of the C-(N)-A-S-H gel remains largely unaltered in sample D (Table 3). After 180 days more Q^2 species are observed in sample B than sample D, while the reverse is true for Q^3(1Al) species. As in the low-Ca samples, increased precursor Al content in sample B results in decreased formation of crosslinking Q^3(1Al) sites, but these do persist to later ages, consistent with thermodynamic modelling of tobermorite-like C-(N)-(A)-S-H in sodium silicate-activated slag [23].

Formation of the additional N-A-S-H gel increases with increased curing time in the Al-rich samples A and B but remains approximately constant low-Al samples C and D (Table 3). Formation of Al-rich N-

A-S-H gel is promoted by increased Al content when Ca content is held constant (as seen in sample A compared with C, and in B compared with D) as well as by reduced Ca content when Al content is held constant (as seen in sample A compared with B, and C compared with D) (Table 3). This is consistent with ^{27}Al MAS NMR observations (section 3.4.1), and also with the known structural limitations [23] on Al substitution within C-(N)-A-S-H gels as it will only substitute into bridging tetrahedral sites; once the Al/Ca ratio surpasses this threshold, the presence of excess Al can result in the formation of a discrete N-A-S-H phase if the Ca content is also not sufficient to accommodate the Al in AFm phases.

The $Q^n(m\text{Al})$ site fractions, MCL, Al/Si ratio and Ca/(Al+Si) ratio of the C-(N)-A-S-H gel formed in each sample can be calculated using the CSTM structural description [23] and are shown in Figure 12 (full details provided in Appendix C, Supporting Information). The MCL (Figure 12a) in samples A and B (bulk Al/Si = 0.15) decreases between 3 and 28 days, and then increases slightly by 180 days. Increased Ca content promotes lower MCL at all ages, consistent with observations for synthetic C-(N)-A-S-H [16]. The MCL in samples C and D (bulk Al/Si = 0.051) increases between 3 and 28 days, and then increases slightly by 180 days in sample C and remains constant in sample D. Increased Ca content again promotes lower MCL at all ages for these low-Al samples.

The Al/Si ratio of C-(N)-A-S-H (Figure 12b) decreases between 3 and 28 days for all samples; increased bulk Al content means that this occurs more rapidly. After 28 days, Al/Si ratio decreases slightly or remains unaltered for samples A and D, whereas it increases for samples B and C, again suggesting an optimum Al/Ca ratio for Al inclusion within the C-(N)-A-S-H gel. Higher bulk Ca content results in reduced Al/Si ratio within the gel at corresponding ages, consistent with FTIR and SEM-EDX observations but contrasting with observations for sodium metasilicate activated slag [21]. Increased bulk Ca content then promotes increased Al/Si ratios within C-(N)-A-S-H at later ages, possibly due to a relative increase in formation of Q^2 and Q^3 type sites which can accommodate more Al inclusion.

Preprint of a paper published in *Cement and Concrete Research*, 89(2016):120-135. Version of record is available at http://dx.doi.org/10.1016/j.cemconres.2016.08.010

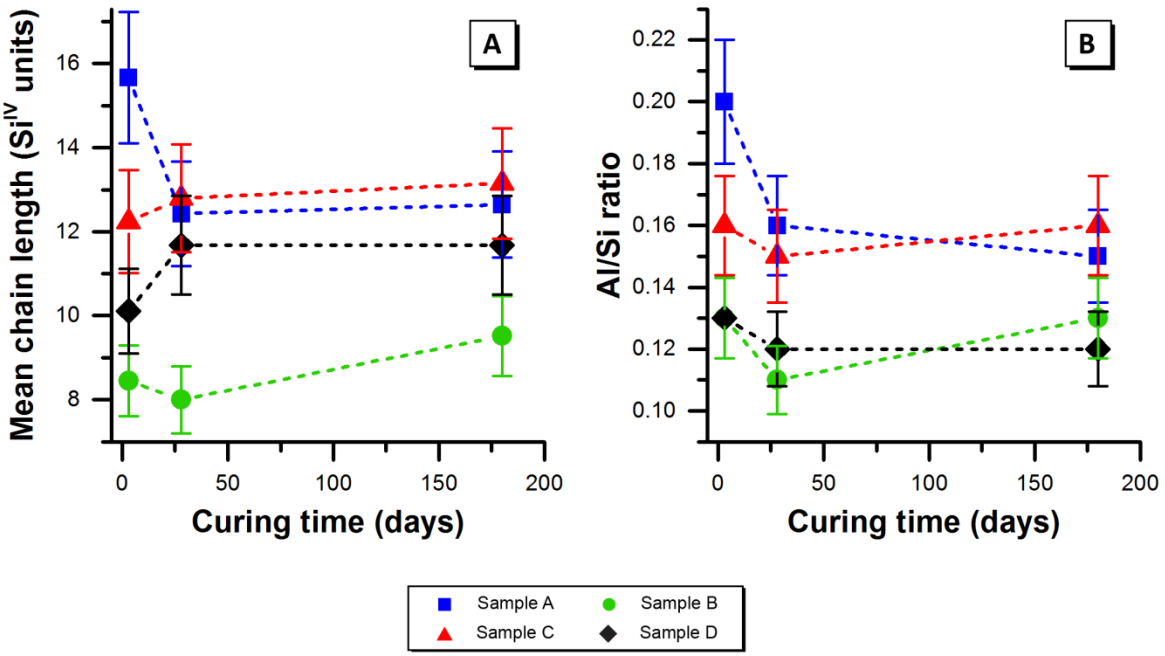

Figure 12: a) Mean chain length and b) Al/Si ratio of the C-(N)-A-S-H gel in each sample calculated from [23]. The estimated uncertainty depicted as error bars is ± 10 % and is due to uncertainty in the absolute site percentages of the ^{29}Si MAS NMR deconvolutions.

3.4.3 ^{23}Na MAS NMR

The ^{23}Na MAS NMR spectra for each AAM exhibit a single broad resonance at approximately −3 ppm (Figure 13). Due to the broad nature of this peak it is attributed to Na^+ cations associated with aluminium-centred tetrahedra in a charge balancing role within both C-(N)-A-S-H [60, 69] and N-A-S-H gel frameworks [10, 70]. This resonance is observed in the spectra of each AAM at all ages, indicating no obvious observable variation in the environments of the charge-balancing Na^+ cations in these binders. A small shoulder at approximately −18 ppm is observed in the ^{23}Na MAS NMR spectra of samples C and D at all timepoints, and is much more pronounced at 28 and 180 days. The position and broad nature of this resonance suggests the presence of Na experiencing much greater electron density than that at −3 ppm, within a very disordered phase, or sorbed to the surfaces of the nanostructured gel.

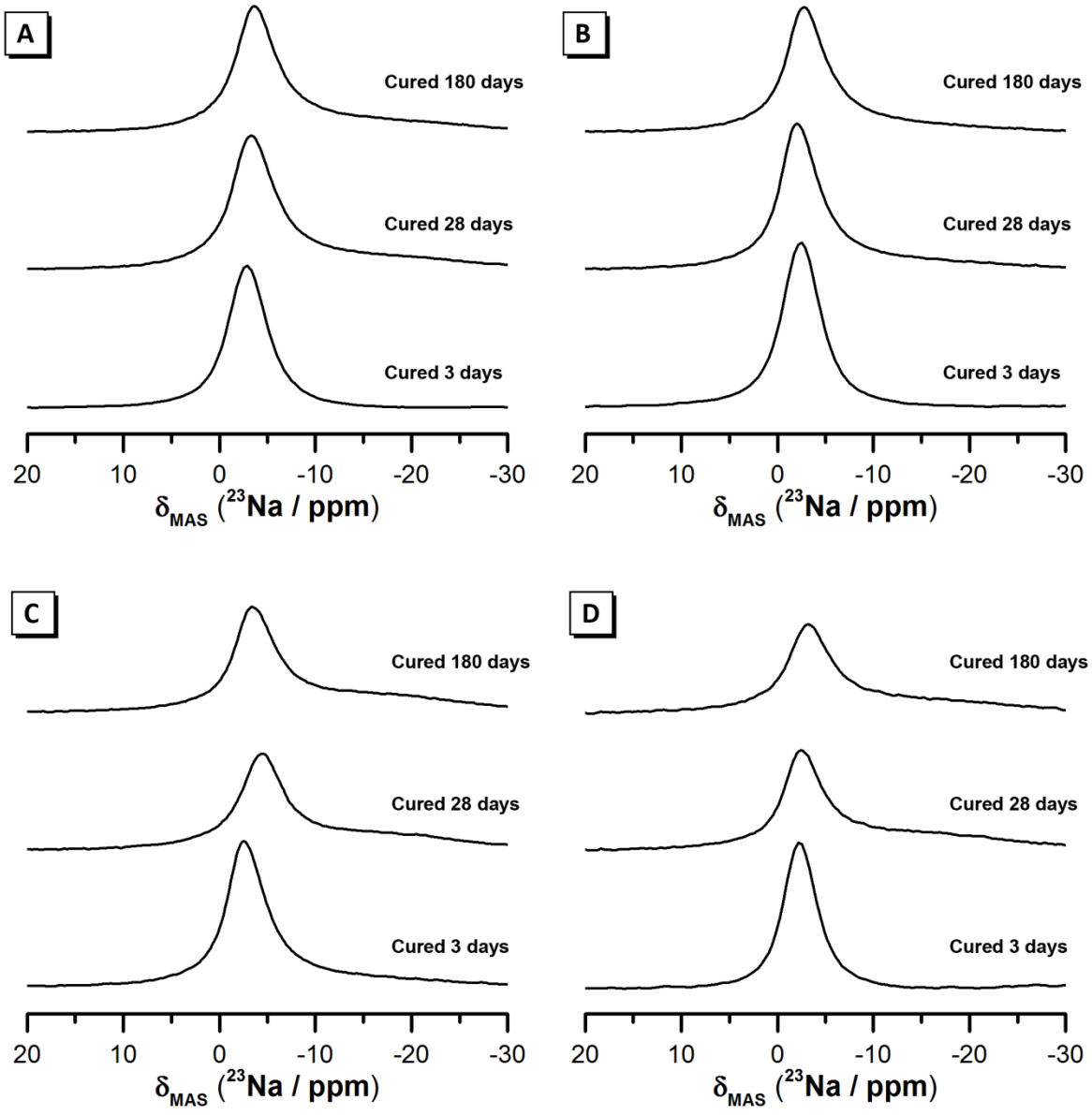

Figure 13: ^{23}Na MAS (12 kHz) NMR (ν_0 = 158.63 MHz) spectra of the alkali-activated material for a) sample A, b) sample B, c) sample C and d) sample D cured for 3, 28 and 180 days as marked.

3.4.4 ^{1}H MAS NMR

The ^{1}H MAS NMR spectra for each sample exhibit broad resonances at approximately 4.5 ppm attributed to intralayer protons within C-(N)-A-S-H (Si-O-H species) [71-73], as well as a low intensity sharp resonance at approximately 0.75 ppm which will contain contributions from resonances due to protons in both portlandite and C-(N)-A-S-H (CaO-H species) [72, 74]. The broad resonance will also

contain a contribution from molecular H_2O adsorbed from the atmosphere [72, 74]. Electron densities surrounding protons within the aluminate hydrates Mc, Hc and C_4AH_{13} will be very similar and consequently these protons are expected to resonate at very similar frequencies. Therefore, the intense, sharp resonance at approximately 1.7 ppm observed in each sample is attributed to protons within chemically bound water in these AFm phases. Although the intensity of this resonance is very small in the spectra for sample C, its presence at all ages indicates that a small amount of an AFm type phase has formed, which was not detectable by XRD or ^{27}Al MAS NMR.

Increased curing time induces an increase in the intensity of the resonance assigned to intralayer protons in C-(N)-A-S-H in all samples, consistent with increased formation of this gel. In samples A, B and D the intensity of the resonance due to the AFm type phases increases significantly at each age of curing, indicating continued formation of these phases and inclusion of water as the reaction progresses, consistent with observations by XRD (section 3.1).

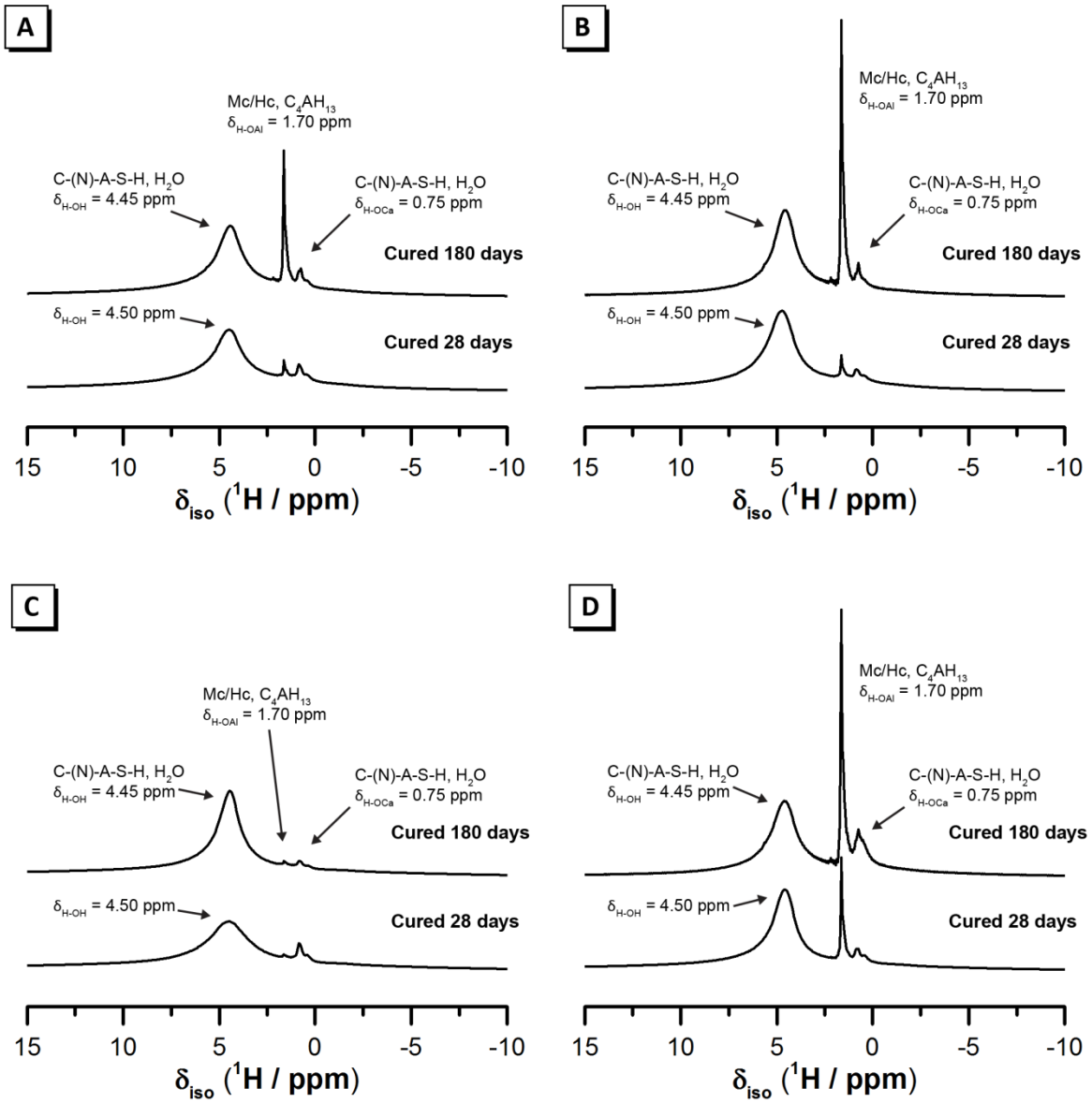

Figure 14: ^{1}H MAS (12 kHz) NMR (ν_0 = 599.70 MHz) spectra of the alkali-activated material for a) sample A, b) sample B, c) sample C and d) sample D cured for 28 and 180 days as marked.

4. Perspectives and Conclusions

Stoichiometrically controlled AAMs were synthesised via alkali-activation of high-purity calcium aluminosilicate precursors which are chemically comparable to the glass in GGBFS. The main reaction product in all samples was a mixed crosslinked/non-crosslinked tobermorite-like C-(N)-A-S-H gel containing varying levels of Al and Na, while additional reaction products were N-A-S-H,

monocarbonate AFm, hemicarbonate AFm, hydroxy-AFm (C_4AH_{13}), the 'third aluminate hydrate' and portlandite. Al within the C-(N)-A-S-H gel substitutes for bridging Si while Na is found in the interlayer, charge-balancing the AlO_4^- tetrahedra and sorbed to the gel surface.

The C-(N)-(A)-S-H and N-A-S-H gel reaction products within these AAMs are chemically and physically similar to those formed within alkali-activated GGBFS, however notable differences in composition and structure of these gels are identified, and correlate strongly with precursor chemical composition. This has important implications when considering alkali-activated binder mix design, particularly when tailoring of physical properties is desired.

Increased Ca content within the reaction mixture promotes greater formation of low-Al, high-Ca containing C-(N)-A-S-H with lower MCL, as well as less formation of AFm type phases, and little evolution of binder chemistry at later ages. The lower Al-binding capacity of crosslinked species led to a decrease in gel crosslinking with increased bulk Al content.

Reduced Ca content and increased Al content in the reaction mixture promote formation of N-A-S-H, in addition to C-(N)-A-S-H and AFm type phases, which exist both as an intimate mixture with C-(N)-A-S-H and as a discrete phase. Increased Al content within C-(N)-A-S-H also results in a decrease in the Ca/Si ratio of the C-(N)-A-S-H gel, and there exists a complex relationship between bulk Ca and Al content and the Al/Si ratio of the C-(N)-A-S-H gel. In general, increased Ca content in the precursor appears to impede formation of N-A-S-H and AFm type phases, and in Al-rich samples (Al/Si= 0.15) results in formation of portlandite in addition to the Al-rich reaction products.

Polymerisation and crosslinking of the C-(N)-A-S-H gel increase with increased curing time. When sufficient levels of Al and alkali are present (Al/Si $\approx$ 0.15), increased curing time also results in increased formation of the additional N-A-S-H gel, due to limitations on the amount of Al substitution possible within the C-(N)-A-S-H gel.

The local coordinations surrounding network forming and modifying cations within these binders, as well as the chemical composition and phases formed, are consistent with those formed by alkali-activation of GGBFS. Consequently, the stoichiometrically controlled AAMs produced in this study constitute a chemically simplified model system through which phase evolution and microstructural development of C-(N)-(A)-S-H and N-A-S-H gels present in alkali activated slag can be further understood. The strong dependence of chemical and physical characteristics of the binders presented here on chemical composition of the reaction mixture highlights the way in which precursor chemistry controls phase evolution and microstructural development of AAMs, and provides a new level of detail in nanostructural insight.

The findings presented in this study show that even small changes in reaction mixture composition can induce significant changes in phase formation and evolution, dictating the microstructure and physical properties of alkali-activated materials. These effects are often competing, with improvements in certain properties coming at the cost of reduced performance in others. This highlights the need to design AAM mix formulations to a specified purpose so that the desired physical properties for a particular application can be achieved. Precursor and reaction mixture composition are therefore important considerations when designing AAM for industrial applications where specific physical properties are desired. Through knowledge of the end use of the material and a thorough understanding of compositional and microstructural changes induced by manipulation of reaction mixture chemistry, as demonstrated within this study, AAM precursors can be designed or selected to produce tailored materials for a wide variety of unique applications.

5. Acknowledgements

This work has been funded in part by the Australian Research Council (ARC), including support through the Particulate Fluids Processing Centre, a Special Research Centre of the ARC. The University of

Melbourne also provided support through an Overseas Research Experience Scholarship to support an extended visit by the first author to the University of Sheffield. We also wish to thank and acknowledge Mr. Roger Curtain, Advanced Microscopy Facility, The University of Melbourne for assistance with scanning electron microscopy experiments.

References

[1] M.C.G. Juenger, F. Winnefeld, J.L. Provis, J.H. Ideker, Advances in alternative cementitious binders, Cem Concr Res, 41 (2011) 1232-1243.

[2] J.L. Provis, A. Palomo, C.J. Shi, Advances in understanding alkali-activated materials, Cem Concr Res, 78 (2015) 110-125.

[3] X.-m. Cui, L.-p. Liu, G.-j. Zheng, R.-p. Wang, J.-p. Lu, Characterization of chemosynthetic Al_2O_3–$2SiO_2$ geopolymers, J Non-Cryst Solids, 356 (2010) 72-76.

[4] I. García-Lodeiro, A. Fernández-Jimenez, A. Palomo, D.E. Macphee, Effect on fresh C-S-H gels of the simultaneous addition of alkali and aluminium, Cem Concr Res, 40 (2010) 27-32.

[5] I. García-Lodeiro, A. Fernández-Jiménez, M.T. Blanco, A. Palomo, FTIR study of the sol–gel synthesis of cementitious gels: C–S–H and N–A–S–H, J Sol-Gel Sci Technol, 45 (2008) 63-72.

[6] I. García-Lodeiro, A. Palomo, A. Fernández-Jiménez, D.E. Macphee, Compatibility studies between N-A-S-H and C-A-S-H gels. Study in the ternary diagram Na_2O–CaO–Al_2O_3–SiO_2–H_2O, Cem Concr Res, 41 (2011) 923-931.

[7] M. Gordon, J.L. Bell, W.M. Kriven, Comparison of naturally and synthetically-derived, potassium based geopolymers, in: Advances in Ceramic Matrix Composites X, John Wiley & Sons, New York, 2004, pp. 95-106.

[8] S.-D. Wang, K.L. Scrivener, ^{29}Si and ^{27}Al NMR study of alkali-activated slag, Cem Concr Res, 33 (2003) 769-774.

[9] S.-D. Wang, K.L. Scrivener, P.L. Pratt, Factors affecting the strength of alkali-activated slag, Cem Concr Res, 24 (1994) 1033-1043.

[10] B. Walkley, R. San Nicolas, M.A. Sani, J.D. Gehman, J.S.J. van Deventer, J.L. Provis, Phase evolution of Na_2O-Al_2O_3-SiO_2-H_2O gels in synthetic aluminosilicate binders, Dalton Trans, 45 (2016) 5521-5535.

[11] B. Walkley, R. San Nicolas, M.A. Sani, J.D. Gehman, J.S.J. van Deventer, J.L. Provis, Synthesis of stoichiometrically controlled reactive aluminosilicate and calcium-aluminosilicate powders, Powder Technol, 297 (2016) 17-33.

[12] H.G. Smolczyk, Slag structure and identification of slags, in: 7th International Congress on the Chemistry of Cement, Paris, France, 1980.

[13] S.A. Bernal, R. San Nicolas, R.J. Myers, R. Mejía de Gutiérrez, F. Puertas, J.S.J. van Deventer, J.L. Provis, MgO content of slag controls phase evolution and structural changes induced by accelerated carbonation in alkali-activated binders, Cem Concr Res, 57 (2014) 33-43.

[14] R.J. Myers, B. Lothenbach, S.A. Bernal, J.L. Provis, Thermodynamic modelling of alkali-activated slag cements, Appl Geochem, 61 (2015) 233-247.

[15] B. Lothenbach, A. Gruskovnjak, Hydration of alkali-activated slag: Thermodynamic modelling, Adv Cem Res, 19 (2007) 81-92.

[16] R.J. Myers, É.M. L'Hôpital, J.L. Provis, B. Lothenbach, Composition-solubility-structure relationships in calcium (alkali) aluminosilicate hydrate (C-(N,K-)A-S-H), Dalton Trans, 44 (2015) 13530-13544.

[17] R.J. Myers, E. L'Hôpital, J.L. Provis, B. Lothenbach, Effect of temperature and aluminium on calcium (alumino)silicate hydrate chemistry under equilibrium conditions, Cem. Concr. Res., 68 (2015) 83-93.

[18] É.M. L'Hôpital, B. Lothenbach, G. Le Saoût, D. Kulik, K. Scrivener, Incorporation of aluminium in calcium-silicate-hydrates, Cem Concr Res, 75 (2015) 91-103.

[19] É.M. L'Hôpital, Aluminium and alkali uptake in calcium silicate hydrates (C-S-H), PhD thesis, École Polytechnique Fédérale de Lausanne, Switzerland, 2014.

[20] B. Walkley, J.L. Provis, R. San Nicolas, M.A. Sani, J.S.J. van Deventer, Stoichiometrically controlled C–(A)–S–H/N–A–S–H gel blends via alkali-activation of synthetic precursors, Adv Appl Ceram, 114 (2015) 372-377.

[21] R.J. Myers, S.A. Bernal, J.D. Gehman, J.S.J. van Deventer, J.L. Provis, The role of Al in cross-linking of alkali-activated slag cements, J Am Ceram Soc, 98 (2015) 996-1004.

[22] R.J. Myers, S.A. Bernal, J.L. Provis, A thermodynamic model for C-(N-)A-S-H gel: CNASH_ss. Derivation and validation, Cem Concr Res, 66 (2014) 27-47.

[23] R.J. Myers, S.A. Bernal, R. San Nicolas, J.L. Provis, Generalized structural description of calcium-sodium aluminosilicate hydrate gels: the cross-linked substituted tobermorite model, Langmuir, 29 (2013) 5294-5306.

[24] A. Fernández-Jiménez, F. Puertas, Structure of calcium silicate hydrates formed in alkaline-activated slag: Influence of the type of alkaline activator, J Am Ceram Soc, 86 (2003) 1389-1394.

[25] G. Le Saoût, M. Ben Haha, F. Winnefeld, B. Lothenbach, Hydration degree of alkali-activated slags: A ^{29}Si NMR study, J Am Ceram Soc, 94 (2011) 4541-4547.

[26] A.R. Brough, A. Atkinson, Sodium silicate-based, alkali-activated slag mortars Part I. Strength, hydration and microstructure, Cem Concr Res, 32 (2002) 865-879.

[27] S.A. Bernal, J.L. Provis, B. Walkley, R. San Nicolas, J.D. Gehman, D.G. Brice, A.R. Kilcullen, P. Duxson, J.S.J. van Deventer, Gel nanostructure in alkali-activated binders based on slag and fly ash, and effects of accelerated carbonation, Cem Concr Res, 53 (2013) 127-144.

[28] G.K. Sun, J.F. Young, R.J. Kirkpatrick, The role of Al in C–S–H: NMR, XRD, and compositional results for precipitated samples, Cem Concr Res, 36 (2006) 18-29.

[29] X. Pardal, I. Pochard, A. Nonat, Experimental study of Si–Al substitution in calcium-silicate-hydrate (C-S-H) prepared under equilibrium conditions, Cem Concr Res, 39 (2009) 637-643.

[30] P. Faucon, A. Delagrave, C. Richet, J.M. Marchand, H. Zanni, Aluminum incorporation in calcium silicate hydrates (C−S−H) depending on their Ca/Si ratio, J Phys Chem B, 103 (1999) 7796-7802.

[31] E. L'Hôpital, B. Lothenbach, D.A. Kulik, K. Scrivener, Influence of calcium to silica ratio on aluminium uptake in calcium silicate hydrate, Cem Concr Res, 85 (2016) 111-121.

[32] É.M. L'Hôpital, B. Lothenbach, K. Scrivener, D.A. Kulik, Alkali uptake in calcium alumina silicate hydrate (C-A-S-H), Cem Concr Res, 85 (2016) 122-136.

[33] I. Ismail, S.A. Bernal, J.L. Provis, S. Hamdan, J.S.J. van Deventer, Drying-induced changes in the structure of alkali-activated pastes, J Mater Sci, 48 (2013) 3566-3577.

[34] F. Delaglio, S. Grzesiek, G. Vuister, G. Zhu, J. Pfeifer, A. Bax, NMRPipe: A multidimensional spectral processing system based on UNIX pipes, J Biomol NMR, 6 (1995) 277-293.

[35] D. Massiot, F. Fayon, M. Capron, I. King, S. Le Calvé, B. Alonso, J.-O. Durand, B. Bujoli, Z. Gan, G. Hoatson, Modelling one- and two-dimensional solid-state NMR spectra, Magn Reson Chem, 40 (2002) 70-76.

[36] J.L. Provis, P. Duxson, G.C. Lukey, J.S.J. van Deventer, Statistical thermodynamic model for Si/Al ordering in amorphous aluminosilicates, Chem Mater, 17 (2005) 2976-2986.

[37] M. Fechtelkord, F. Stief, J.-C. Buhl, Sodium cation dynamics in nitrate cancrinite: A low and high temperature ^{23}Na and ^{1}H MAS NMR study and high temperature Rietveld structure refinement, Am Miner, 86 (2001) 165-175.

[38] B. Lothenbach, G. Le Saoût, E. Gallucci, K. Scrivener, Influence of limestone on the hydration of Portland cements, Cem Concr Res, 38 (2008) 848-860.

[39] T. Matschei, B. Lothenbach, F.P. Glasser, The AFm phase in Portland cement, Cem Concr Res, 37 (2007) 118-130.

[40] S.-Y. Hong, F.P. Glasser, Alkali binding in cement pastes: Part I. The C-S-H phase, Cem Concr Res, 29 (1999) 1893-1903.

[41] S.-Y. Hong, F.P. Glasser, Alkali sorption by C-S-H and C-A-S-H gels: Part II. Role of alumina, Cem Concr Res, 32 (2002) 1101-1111.

[42] J. Duchesne, M.A. Bérubé, The effectiveness of supplementary cementing materials in suppressing expansion due to ASR: Another look at the reaction mechanisms part 2: Pore solution chemistry, Cem Concr Res, 24 (1994) 221-230.

[43] M. Codina, C. Cau-dit-Coumes, P. Le Bescop, J. Verdier, J.P. Ollivier, Design and characterization of low-heat and low-alkalinity cements, Cem Concr Res, 38 (2008) 437-448.

[44] B. Lothenbach, K. Scrivener, R.D. Hooton, Supplementary cementitious materials, Cem Concr Res, 41 (2011) 1244-1256.

[45] L. Fernández-Carrasco, E. Vázquez, Reactions of fly ash with calcium aluminate cement and calcium sulphate, Fuel, 88 (2009) 1533-1538.

[46] H.J. Kuzel, H. Pöllmann, Hydration of C_3A in the presence of $Ca(OH)_2$, $CaSO_4{\cdot}2H_2O$ and $CaCO_3$, Cem Concr Res, 21 (1991) 885-895.

[47] R. Snellings, T. Paulhiac, K. Scrivener, The effect of Mg on slag reactivity in blended cements, Waste Biomass Valor, 5 (2014) 369-383.

[48] D. Damidot, S. Stronach, A. Kindness, M. Atkins, F.P. Glasser, Thermodynamic investigation of the $CaO{\cdot}Al_2O_3{\cdot}CaCO_3{\cdot}H_2O$ closed system at 25°C and the influence of Na_2O, Cem Concr Res, 24 (1994) 563-572.

[49] P. Yu, R.J. Kirkpatrick, B. Poe, P.F. McMillan, X. Cong, Structure of calcium silicate hydrate (C-S-H): Near-, mid-, and far-infrared spectroscopy, J Am Ceram Soc, 82 (1999) 742-748.

[50] S.A. Bernal, J.L. Provis, V. Rose, R. Mejía de Gutiérrez, Evolution of binder structure in sodium silicate-activated slag-metakaolin blends, Cem Concr Compos, 33 (2011) 46-54.

[51] S.A. Bernal, R. Mejía de Gutiérrez, J.L. Provis, V. Rose, Effect of silicate modulus and metakaolin incorporation on the carbonation of alkali silicate-activated slags, Cem Concr Res, 40 (2010) 898-907.

[52] I. Ismail, S.A. Bernal, J.L. Provis, R. San Nicolas, S. Hamdan, J.S.J. van Deventer, Modification of phase evolution in alkali-activated blast furnace slag by the incorporation of fly ash, Cem Concr Compos, 45 (2014) 125-135.

[53] J.A. Gadsden, Infrared spectra of minerals and related inorganic compounds, Butterworths, London, 1975.

[54] V.C. Farmer, The Infrared spectra of minerals, Mineralogical Society, London, 1974.

[55] I.G. Richardson, The nature of C-S-H in hardened cements, Cem Concr Res, 29 (1999) 1131-1147.

[56] A.L. Gameiro, A.S. Silva, M.d.R. Veiga, A.L. Velosa, Lime-metakaolin hydration products: A microscopy analysis, Mater Technol, 46 (2012) 145-148.

[57] R.R. Lloyd, J.L. Provis, J.S.J. van Deventer, Microscopy and microanalysis of inorganic polymer cements. 1: remnant fly ash particles, J Mater Sci, 44 (2009) 608-619.

[58] J.S.J. van Deventer, R. San Nicolas, I. Ismail, S.A. Bernal, D.G. Brice, J.L. Provis, Microstructure and durability of alkali-activated materials as key parameters for standardization, J Sust Cem-Based Mater, 4 (2014) 116-128.

[59] P. Pena, J.M. Rivas Mercury, A.H. de Aza, X. Turrillas, I. Sobrados, J. Sanz, Solid-state ^{27}Al and ^{29}Si NMR characterization of hydrates formed in calcium aluminate–silica fume mixtures, J Solid State Chem, 181 (2008) 1744-1752.

[60] F. Bonk, J. Schneider, M.A. Cincotto, H.c. Panepucci, Characterization by multinuclear high-resolution NMR of hydration products in activated blast-furnace slag pastes, J Am Ceram Soc, 86 (2003) 1712-1719.

[61] M.D. Andersen, H.J. Jakobsen, J. Skibsted, Incorporation of aluminum in the calcium silicate hydrate (C−S−H) of hydrated Portland cements: A high-field ^{27}Al and ^{29}Si MAS NMR investigation, Inorg Chem, 42 (2003) 2280-2287.

[62] E.H. Oelkers, S.R. Gislason, The mechanism, rates and consequences of basaltic glass dissolution: I. An experimental study of the dissolution rates of basaltic glass as a function of aqueous Al, Si and oxalic acid concentration at 25°C and pH = 3 and 11, Geochim Cosmochim Acta, 65 (2001) 3671-3681.

[63] M.D. Andersen, H.J. Jakobsen, J. Skibsted, A new aluminium-hydrate species in hydrated Portland cements characterized by ^{27}Al and ^{29}Si MAS NMR spectroscopy, Cem Concr Res, 36 (2006) 3-17.

[64] R. Taylor, I.G. Richardson, R.M.D. Brydson, Composition and microstructure of 20-year-old ordinary Portland cement–ground granulated blast-furnace slag blends containing 0 to 100% slag, Cem Concr Res, 40 (2010) 971-983.

[65] S.D. Wang, K.L. Scrivener, Hydration products of alkali-activated slag cement, Cem Concr Res, 25 (1995) 561-571.

[66] J.L. Provis, J.S.J. van Deventer (eds.), Alkali Acivated Materials. State-of-the-Art Report, RILEM TC 224-AAM, Springer, Dordrecht, 2014.

[67] I.G. Richardson, The calcium silicate hydrates, Cem Concr Res, 38 (2008) 137-158.

[68] J. Brus, L. Kobera, M. Urbanová, D. Koloušek, J. Kotek, Insights into the structural transformations of aluminosilicate inorganic polymers: A comprehensive solid-state NMR study, J Phys Chem C, 116 (2012) 14627-14637.

[69] H. Viallis, P. Faucon, J.C. Petit, A. Nonat, Interaction between salts (NaCl, CsCl) and calcium silicate hydrates (C−S−H), J Phys Chem B, 103 (1999) 5212-5219.

[70] P. Duxson, G.C. Lukey, F. Separovic, J.S.J. van Deventer, Effect of alkali cations on aluminum incorporation in geopolymeric gels, Ind Eng Chem Res, 44 (2005) 832-839.

[71] G. Renaudin, J. Russias, F. Leroux, C. Cau-dit-Coumes, F. Frizon, Structural characterization of C–S–H and C–A–S–H samples—Part II: Local environment investigated by spectroscopic analyses, J Solid State Chem, 182 (2009) 3320-3329.

[72] F. Méducin, B. Bresson, N. Lequeux, M.N.d. Noirfontaine, H. Zanni, Calcium silicate hydrates investigated by solid-state high resolution ^{1}H and ^{29}Si nuclear magnetic resonance, Cem Concr Res, 37 (2007) 631-638.

[73] B. Bresson, S. Masse, H. Zanni, C. Noik, Tricalcium silicate hydration at high temperature. A ^{29}Si and ^{1}H NMR Investigation, in: P. Colombet, A.-R. Grimmer, H. Zanni, P. Sozzani (Eds.) Nuclear Magnetic Resonance Spectroscopy of Cement-Based Materials, Springer, Berlin Heidelberg, 1998, pp. 209-215.

[74] D. Heidemann, W. Wieker, Characterization of protons in C-S-H phases by means of high-speed ^{1}H MAS NMR investigations, in: P. Colombet, A.-R. Grimmer, H. Zanni, P. Sozzani (Eds.) Nuclear Magnetic Resonance Spectroscopy of Cement-Based Materials, Springer, Berlin Heidelberg, 1998, pp. 169-180.

[75] V.R. Zivica, A. Bajza, Acidic attack of cement based materials — a review. Part 1. Principle of acidic attack, Constr Build Mater, 15 (2001) 331-340.

[76] C. Shi, Z. Shi, X. Hu, R. Zhao, L. Chong, A review on alkali-aggregate reactions in alkali-activated mortars/concretes made with alkali-reactive aggregates, Mater Struct, 48 (2015) 621-628.

[77] I. Ismail, S.A. Bernal, J.L. Provis, R. San Nicolas, D.G. Brice, A.R. Kilcullen, S. Hamdan, J.S.J. van Deventer, Influence of fly ash on the water and chloride permeability of alkali-activated slag mortars and concretes, Constr Build Mater, 48 (2013) 1187-1201.

[78] C. Shi, Corrosion resistance of alkali-activated slag cement, Adv Cem Res, 15 (2003) 77-81.

[79] M.D.A. Thomas, The effect of supplementary cementing materials on alkali-silica reaction: A review, Cem Concr Res, 41 (2011) 1224-1231.